Chapter 15

Decoherence, refocusing and dynamical decoupling of spin qubits

A spin degree of freedom is a robust qubit candidate due to its extremely weak coupling to external reservoirs if we compare it to other degrees of freedom such as a charge degree of freedom. However, a very fact that we can manipulate a spin qubit with an external control force indicates that a spin qubit still couples to external degrees of freedom and loses its quantum coherence with a finite time. In this chapter we will study the decoherence properties of a spin qubit and several pulse techniques to eliminate such an extrinsic decoherence effect.

15.1 Decoherence of spin qubits

15.1.1 Transverse relaxation (T_2) process [1, 2]

A spin qubit loses its phase information by a fluctuating magnetic field along z-axis (quantization axis). The relevant interaction for this particular decoherence process is abstractly represented by the Zeeman Hamiltonian:

$$\hat{\mathcal{H}} = -\gamma\hbar\left[H_0 + \Delta H(t)\right]\hat{I}_z = -\hbar\left[\omega_0 + \Delta\omega(t)\right]\hat{I}_z \quad . \tag{15.1}$$

Here H_0 is a *dc* magnetic field along z-axis, $\omega_0 = \gamma H_0$ is the Larmor frequency of a spin, $\Delta H(t)$ is a fluctuating magnetic field along z-axis and $\Delta\omega(t) = \gamma\Delta H(t)$ is a corresponding frequency (modulation) noise. The origin of $\Delta H(t)$ might be a paramagnetic impurity near a spin qubit or surrounding nuclear spin bath or stray magnetic field.

Suppose the initial spin state is given by

$$|\psi(0)\rangle = \frac{1}{\sqrt{2}}\left(|\uparrow\rangle + |\downarrow\rangle\right) \quad , \tag{15.2}$$

the final state after a free evolution according to (15.1) is

$$|\psi(t)\rangle = \frac{1}{\sqrt{2}}\left(e^{-i\frac{\omega_0}{2}t}e^{-\frac{i}{2}\int_0^t\Delta\omega(t')dt'}|\uparrow\rangle + e^{i\frac{\omega_0}{2}t}e^{\frac{i}{2}\int_0^t\Delta\omega(t')dt'}|\downarrow\rangle\right) \quad , \tag{15.3}$$

If we move from a laboratory frame to a rotating frame, in which $x-y$ axis rotates along z-axis with an angular frequency ω_0, (15.3) can be expressed as

$$|\psi(t)\rangle = \frac{1}{\sqrt{2}}\left(e^{-\frac{1}{2}\Delta\phi(t)}|\uparrow\rangle + e^{\frac{1}{2}\Delta\phi(t)}|\downarrow\rangle\right) \quad , \tag{15.4}$$

where

$$\Delta\phi(t) = \int_0^t \Delta\omega(t')dt' \quad . \tag{15.5}$$

If an instantaneous Larmor frequency noise $\Delta\omega(t)$ has an infinitesimally short correlation time, its noise spectrum $S_{\Delta\omega}(\Omega)$ becomes a white noise and the resulting phase noise given by (15.5) features a non-stationary random walk diffusion as shown in Fig. 15.1. This is a Wiener-Levy process studied in Chapter 1.

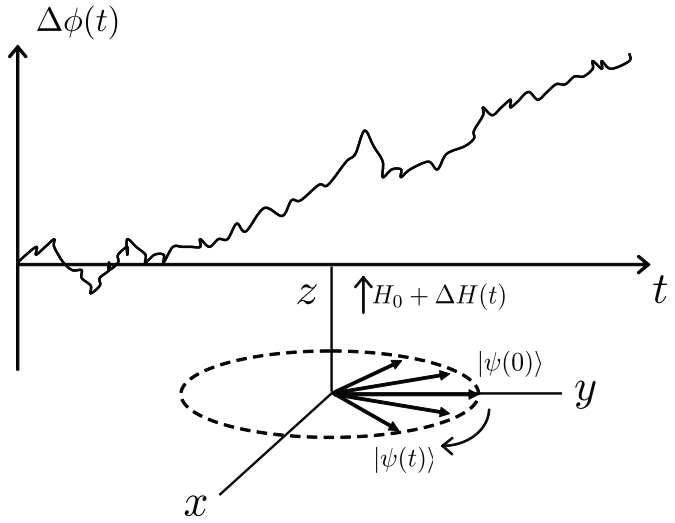

Figure 15.1: A random walk of a phase $\Delta\phi(t)$ of a spin qubit $|\psi(t)\rangle$ due to a fluctuating magnetic field $\Delta H(t)$.

By introducing a gated function between $[0, T]$, we can employ the Fourier analysis. A co-variance function for the phase noise is defined by

$$\langle\Delta\phi(t+\tau)\Delta\phi(t)\rangle = \int_0^{t+\tau}\int_0^t \langle\Delta\omega(t')\Delta\omega(t")\rangle dt'dt" \quad . \tag{15.6}$$

Since an instaneous frequency noise $\Delta\omega(t)$ is a statistically stationary and ergodic process, we can replace the ensemble average in the right hand side of (15.6) with the time average,

$$\begin{aligned} \langle\Delta\omega(t')\Delta\omega(t")\rangle &= \lim_{T\to\infty}\frac{1}{T}\int_{-\frac{T}{2}}^{\frac{T}{2}} \Delta\omega(t+\tau)\Delta\omega(t)dt \\ &= \frac{1}{2\pi}\int_0^\infty S_{\Delta\omega}(\Omega)\cos(\Omega\tau)d\Omega \quad . \end{aligned} \tag{15.7}$$

Here $\tau = t' - t"$ and we used the Wiener-Khintchine theorem. From (15.6) and (15.7), we have

$$\langle\Delta\phi(t+\tau)\Delta\phi(t)\rangle = \frac{1}{2\pi}\int_0^\infty d\Omega S_{\Delta\omega}(\Omega)\int_0^{t+\tau} dt'\int_0^t dt" \cos\left[\Omega(t'-t")\right] \tag{15.8}$$

$$= \frac{1}{2\pi}\int_0^\infty d\Omega S_{\Delta\omega}(\Omega)\frac{1}{\Omega^2}\left\{1+\cos(\Omega\tau)-\cos(\Omega t)-\cos\left[\Omega(t+\tau)\right]\right\} \quad .$$

By setting $\tau = 0$, we can obtain the variance of the phase noise:

$$\begin{aligned}\langle\Delta\phi(t)^2\rangle &= \frac{1}{\pi}S_{\Delta\omega}(\Omega\sim 0)\int_0^\infty d\Omega\frac{1}{\Omega^2}\left[1-\cos(\Omega t)\right], \qquad (15.9)\\ &= \frac{1}{2}S_{\Delta\omega}(\Omega\sim 0)t \quad ,\end{aligned}$$

where we use the fact that $S_{\Delta\omega}(\Omega)$ is a white noise so that $S_{\Delta\omega(\Omega)}$ can be replaced by its zero-frequency spectral density $S_{\Delta\omega}(\Omega\simeq 0)$. If we introduce a phase diffusion constant $D_{\Delta\phi}$ by

$$\langle\Delta\phi(t)^2\rangle = 2D_{\Delta\phi}t \quad , \qquad (15.10)$$

the phase diffusion constant is uniquely determined by the zero frequency spectral density $S_{\Delta\omega}(\Omega\simeq 0)$ of an instantaneous frequency,

$$D_{\Delta\phi} = \frac{1}{4}S_{\Delta\omega}(\Omega\simeq 0) \quad . \qquad (15.11)$$

The 2×2 density matrix of the initial spin state (15.2) is expressed as

$$\hat{\rho} = \begin{pmatrix}\rho_{\uparrow\uparrow} & \rho_{\uparrow\downarrow}\\ \rho_{\downarrow\uparrow} & \rho_{\downarrow\downarrow}\end{pmatrix} = \frac{1}{2}\begin{pmatrix}1 & 1\\ 1 & 1\end{pmatrix} \quad . \qquad (15.12)$$

The instantaneous frequency noise $\Delta\omega(t)$ does not decay the diagonal terms $\rho_{\uparrow\uparrow}$ and $\rho_{\downarrow\downarrow}$ but decays the off-diagonal terms,

$$\begin{aligned}\rho_{\uparrow\downarrow}(t) = \rho_{\downarrow\uparrow}(t) &= \frac{1}{2}\langle e^{i\Delta\phi(t)}\rangle \qquad (15.13)\\ &= \frac{1}{2}\exp\left\{-\frac{1}{2}\langle\Delta\phi(t)^2\rangle\right\}\\ &= \frac{1}{2}\exp\left[-D_{\Delta\phi}(t)\right] \quad .\end{aligned}$$

The off-diagonal term decays exponentially with a time constant $T_2 = \frac{1}{D_{\Delta\phi}} = \frac{4}{S_{\Delta\omega}(\Omega\simeq 0)}$. Since the instantaneous frequency noise $\Delta\omega(t)$ is proportional to the magnetic field fluctuation $\Delta H(t)$, the zero-frequency spectral density of $\Delta H(t)$ ultimately determines the magnitude of a phase coherence time T_2.

Remark:

1. In real experimental situations, the instantaneous frequency noise $\Delta\omega(t)$ has a varying spectral shape depending on magnetic environments. Often, $1/f$ noise dominates at low frequencies due to the distributed random telegraphic signals as discussed in chapter 9. At high frequencies, quantum zero-point fluctuations proportion to frequency ω always dominate, as discussed in chapter 4. We must evaluate

$$\langle\Delta\phi(t)^2\rangle = \frac{1}{\pi}\int_0^\infty d\Omega S_{\Delta\omega}(\Omega)\frac{1}{\Omega^2}\left[1-\cos(\Omega t)\right] \quad , \qquad (15.14)$$

instead of (15.9) to calculate the decay of the off-diagonal elements $\rho_{\uparrow\downarrow}$ and $\rho_{\downarrow\uparrow}$.

2. An applied *dc* field H_0 is not completely uniform in all space points. If many spin qubits are placed in such an inhomogeneous *dc* field, they have different Larmor frequencies. This leads to the dephasing effect if we compare the phase difference between different qubits. A time constant for this dephasing process is determined by the spatial (not temporal) inhomogeneous broadening of the *dc* field and distinguished from T_2 process. A new time constant is often referred to as T_2^*.

15.1.2 Longitudinal relaxation (T_1) process [3]

A spin qubit loses its amplitude information by a fluctuating transverse magnetic field in a $x-y$ plane. The relevant interaction for this particular spin relaxation process is abstractly represented by the spin-boson Hamiltonian:

$$\hat{\mathcal{H}} = -\gamma\hbar H_0 \hat{I}_z + \sum_s \hbar\omega_s \left(\hat{a}_s^+ \hat{a}_s + 1/2\right) - \sum_s \hbar g_s \left(\hat{I}_+ \hat{a}_s + \hat{I}_- \hat{a}_s^+\right) \quad , \tag{15.15}$$

where $\hat{a}_s$ ($\hat{a}_s^+$) is the boson annihilation (creation) operator which represent a transverse *ac* magnetic field. The third term represents the spin flip process by absorbing or emitting one photon.

Suppose the initial spin state is given by

$$|\psi(0)\rangle = |\uparrow\rangle_s |0\rangle_f \quad , \tag{15.16}$$

where the spin is in an excited state $|\uparrow\rangle_s$ and the field is a vacuum state $|0\rangle_f$. The final state is of the form

$$|\psi(t)\rangle = C_{\uparrow 0}(t) e^{-i\frac{\omega_0}{2}t} |\uparrow, 0\rangle + \sum_s C_{\downarrow s}(t) e^{i\left(\frac{\omega_0}{2}-\omega_s\right)t} |\downarrow, s\rangle \quad , \tag{15.17}$$

where $|\downarrow, s\rangle$ represents a state in which the spin is in a ground state $|\downarrow\rangle_s$ and the field mode s acquires one photon $|1\rangle_s$. Note that the field modes have continuous spectrum so that all the other modes except for a particular mode s remain vacuum states. The final state (15.17) should satisfy the Schödinger equation,

$$i\hbar \frac{d}{dt}|\psi(t)\rangle = \hat{\mathcal{H}}|\psi(t)\rangle \quad . \tag{15.18}$$

By substituting (15.17) into (15.18) and projecting $\langle\uparrow, 0|$ and $\langle\downarrow, s|$ on both sides of the resulting equation, we obtain the coupled mode equations:

$$\dot{C}_{\uparrow 0}(t) = -i \sum_s g_s e^{-i(\omega_s-\omega_0)t} C_{\downarrow s}(t) \quad , \tag{15.19}$$

$$\dot{C}_{\downarrow s}(t) = -i g_s e^{i(\omega_s-\omega_0)t} C_{\uparrow 0}(t) \quad . \tag{15.20}$$

The formal integration of (15.20) with an initial condition of $C_{\downarrow s}(0) = 0$ results in

$$C_{\downarrow s}(t) = -i g_s \int_0^t dt' e^{i(\omega_s-\omega_0)t'} C_{\uparrow 0}(t') \quad . \tag{15.21}$$

If we substitute (15.21) into (15.19), we have the following integro-differential equation for $C_{\uparrow 0}(t)$:

$$\dot{C}_{\uparrow 0}(t) = \sum_s g_s^2 \int_0^t dt' e^{-i(\omega_s - \omega_0)(t-t')} C_{\uparrow 0}(t') \quad . \tag{15.22}$$

The summation over all field modes $\sum_s$ can be replaced by the integral with the energy density of states in a reasonably large volume,

$$\sum_s g_s^2 \to \int_0^\infty d\omega_s g\left(\omega_s\right)^2 \rho\left(\omega_s\right) \quad . \tag{15.23}$$

In a very short time scale, we can safely assume $C_{\uparrow 0}(t')$ in (15.22) satisfies

$$C_{\uparrow 0}(t') \simeq C_{\uparrow 0}(0) = 1 \quad . \tag{15.24}$$

Then, (15.22) is reduced to

$$\begin{aligned} \dot{C}_{\uparrow 0}(t) = &= -\int_0^\infty d\omega_s g\left(\omega_s\right)^2 \rho\left(\omega_s\right) \int_0^t dt' e^{-i(\omega_s - \omega_0)(t-t')} \\ &= -\int_0^\infty d\omega_s g\left(\omega_s\right)^3 \rho\left(\omega_s\right) \left[\pi\delta\left(\omega_s - \omega_0\right) - P\left(\frac{i}{\omega_s - \omega_0}\right)\right] \\ &= -\frac{\Gamma}{2} - i\delta\omega \quad , \end{aligned} \tag{15.25}$$

where

$$\Gamma = 2\pi g\left(\omega_0\right)^2 \rho\left(\omega_0\right) \quad , \tag{15.26}$$

$$\delta\omega = P\left[\int_0^\infty \frac{g\left(\omega_s\right)^2 \rho\left(\omega_s\right)}{\omega_s - \omega_0} d\omega\right] \quad , \tag{15.27}$$

where P stands for a principle value. Thus, the probability amplitude for finding the initial state is given by

$$C_{\uparrow 0}(t) = 1 - \left(\frac{\Gamma}{2} + i\delta\omega\right) t \quad . \tag{15.28}$$

Γ is the Fermi golden rule decay rate of the excited state and $\delta\omega$ is a frequency shift.

In a very long time scale, we cannot replace $C_{\uparrow 0}(t')$ by $C_{\uparrow 0}(0)$ but we can still approximate $C_{\uparrow 0}(t')$ by $C_{\uparrow 0}(t)$ in (15.22). This is because the bosonic reservoir frequency ω_s is very broadly distributed over ω_0 so that the time integral in (15.22) has a non-zero contribution only if $t' \simeq t$. If we replace $C_{\uparrow 0}(t')$ in (15.22) by $C_{\uparrow 0}(t)$, we have

$$\dot{C}_{\uparrow 0}(t) = \left(-\frac{\Gamma}{2} - i\delta\omega\right) C_{\uparrow 0}(t) \quad . \tag{15.29}$$

The solution of the above differential equation has an exponential form:

$$C_{\uparrow 0}(t) = \exp\left[\left(-\frac{\Gamma}{2} - i\delta\omega\right) t\right] \quad . \tag{15.30}$$

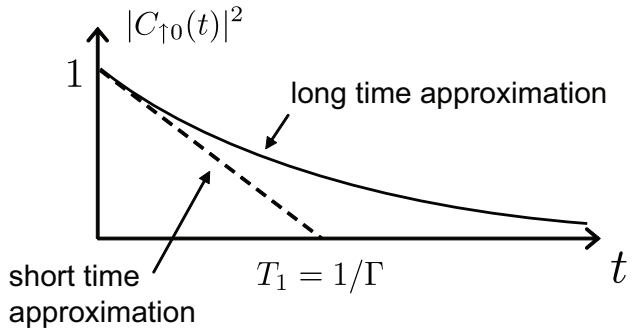

Figure 15.2: The decay of $|C_{\uparrow 0}(t)|^2$ by short time and long time approximation.

Remark:

1. The Fourier transform of (15.30) provides the spectrum (frequency distribution) of the final state $|\downarrow, s\rangle$:

$$S(\omega_s) \propto \frac{1}{[\omega_s - (\omega_0 + \delta\omega)]^2 + \left(\frac{\Gamma}{2}\right)^2} \quad . \tag{15.31}$$

   The spectrum features a Lorentzian line shape with a full width at half maximum $\Gamma = 1/T_1$. This linewidth is called a natural linewidth and places a theoretical limit on the decoherence of a spin qubit $T_2 = 2T_1$.

2. The above approximation used in a long time scale is called the Weisskopf-Wigner approximation and is valid as far as the frequency interval Δ, over which $g(\omega_s)^2 \rho(\omega_s)$ has an appreciable value, is much greater than the natural linewidth Γ as shown below.

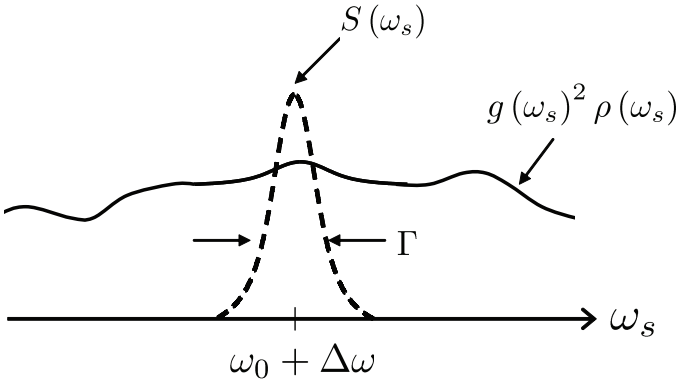

Figure 15.3: Distribution of $g(\omega_s)^2 \rho(\omega_s)$ and final state $S(\omega_s)$.

3. If $g(\omega_s)^2 \rho(\omega_s)$ has a discrete spectrum rather than a continuous spectrum, $|C_{\uparrow 0}(t)|^2$ decays but reappears at a later time due to constructive interference of the recoupling from different paths $C_{\downarrow s}(t)$. This is called a Cumming's revival.

4. In contrast to the spin decoherence (T_2) process mainly contributed by the near zero frequency component of the longitudinal magnetic field fluctuation, the spin relaxation (T_1) process is mainly caused by the near Larmor frequency component of the transverse magnetic field fluctuation.

15.2 Refocusing of spin qubits

15.2.1 Hahn's spin echo

Figure 15.4 shows the principle of Hahn's spin echo. A spin is initially oriented along $+z$ direction (Fig. 15.4(a)). By applying a transverse rf field with a pulse area of $\pi/2$ along $x-$ axis, the spin is flipped along $-y$ direction, in which we assume a negative gyromagnetic ratio $\gamma < 0$ (Fig. 15.4(b)). After a free evolution over a time τ, the spin may acquire an advanced phase or delayed phase if the particular spin has a Larmor frequency of more than or less than the average value which determines a rotating reference frame (Fig. 15.4(c)). We send a refocusing pulse of area π along $x-$axis so that the spin is rotated by 180° around $x-$ axis (Fig. 15.4(d)). If we let the spin precess freely for the same period of τ, the spin with an advanced phase or a delayed phase can be refocused onto the $+y$ direction (Fig. 15.4(e)). Therefore, the magnetic resonance signal disappears once due to dephasing effect, but if a π-pulse is sent at $t = \tau$, the signal reappears at $t = 2\tau$. This second signal is called a spin echo signal (Fig. 15.5)

Next we will describe the Hahn's spin echo in Schrödinger picture. The Schrödinger equation in a rotating reference frame is

$$i\hbar \frac{d}{dt}|\psi(t)\rangle = \hat{\mathcal{H}}|\psi(t)\rangle \quad , \tag{15.32}$$

where

$$\hat{\mathcal{H}} = -\gamma\hbar \left(h_0 \hat{I}_z + H_1 \hat{I}_x \right) \quad . \tag{15.33}$$

Here $h_0 = H_{loc} - \frac{\omega}{\gamma}$ represents the distribution of inhomogeneous local dc field H_{loc}. We assume the distribution of H_{loc} is much smaller than the spectrum of transverse rf field pulse so that every spin is identically rotated by either $\pi/2$ or π.

This assumption is called a "hard pulse" or "short pulse". Due to this assumption we can safely separate the effective Hamiltonian as

$$\hat{\mathcal{H}} = \begin{cases} -\gamma\hbar H_1 \hat{I}_x & \text{(during pulse excitation)} \\ -\gamma\hbar h_0 \hat{I}_z & \text{(free evolution)} \end{cases} \quad . \tag{15.34}$$

The spin evolution by the first $\pi/2$ pulse is described by

$$|\psi(t_1)\rangle = e^{i\gamma H_1 t_1 \hat{I}_x}|\psi(0)\rangle = \hat{X}(\pi/2)|\psi(0)\rangle \quad . \tag{15.35}$$

This unitary oeprator $\hat{X}(\pi/2)$ represents the spin rotation about $x-$ axis by an angle $\theta = \gamma H_1 t_1 = \pi/2$. The free evolution between $t = t_1$ and t_2 is described by

$$|\psi(t_2)\rangle = e^{i\gamma h_0 (t_2 - t_1)\hat{I}_z}|\psi(t_1)\rangle = \hat{T}(\tau, h_0)|\psi(t_1)\rangle \quad . \tag{15.36}$$

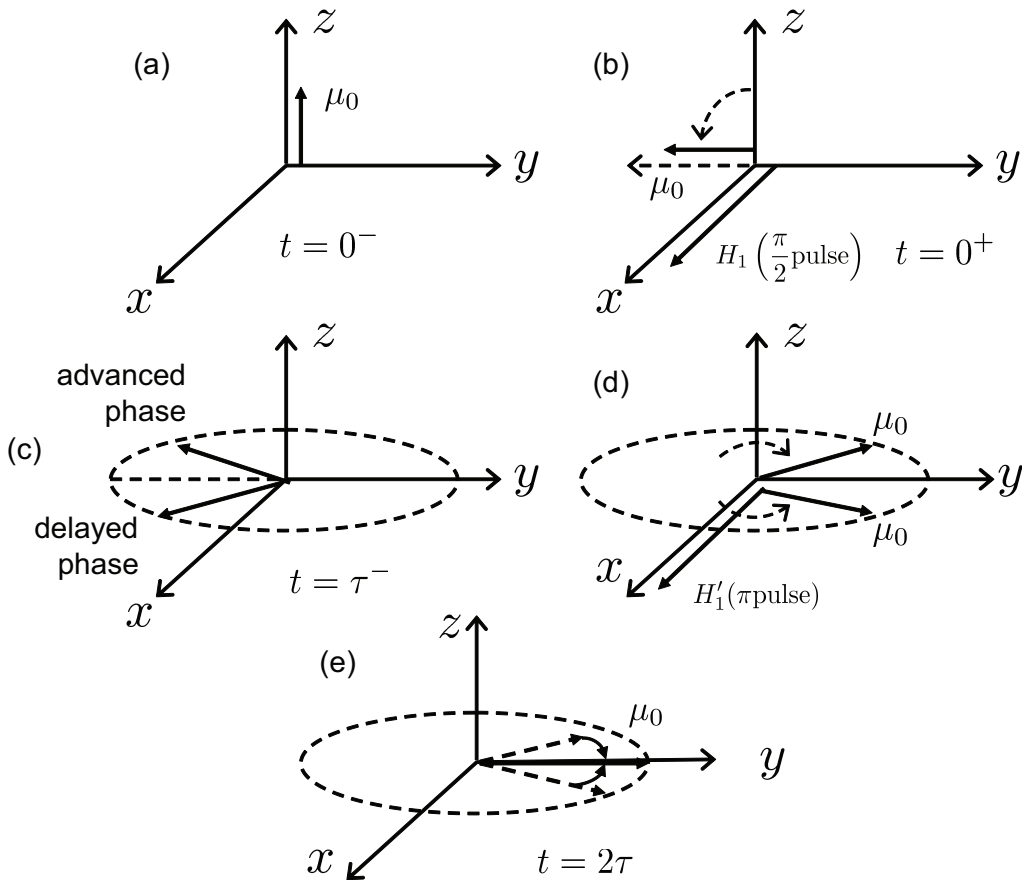

Figure 15.4: The principle of Hahn's spin echo.

The above unitary operator represents the spin rotation about $z-$ axis by an angle of $\alpha = \gamma h_0 \tau$. Then, we send the π pulse and let the spin systems evolve freely over a time $t - \tau$, which results in

$$|\psi(t)\rangle = \hat{T}(t-\tau, h_0)\hat{X}(\pi)\hat{T}(\tau, h_0)\hat{X}(\pi/2)|\psi(0)\rangle \quad . \tag{15.37}$$

We then measure the spin component along $y-$ axis by a homodyne detector and the expected signal can be calculated by

$$\langle \hat{I}_y \rangle = \int P(h_0) dh_0 \langle \psi(t)|\hat{I}_y|\psi(t)\rangle \quad , \tag{15.38}$$

where $P(h_0)$ is the distribution of the Larmor frequencies.

In order to proceed, we can use the following spin transformation by $\pi/2$ pulse and π pulse for $\gamma < 0$ (right handed system):

$$\begin{aligned} \hat{X}^{-1}(\pi/2)\hat{I}_y\hat{X}(\pi/2) &= \hat{I}_z \\ \hat{X}^{-1}(\pi/2)\hat{I}_z\hat{X}(\pi/2) &= -\hat{I}_y \\ \hat{X}^{-1}(\pi/2)\hat{I}_x\hat{X}(\pi/2) &= \hat{I}_x \quad , \end{aligned} \tag{15.39}$$

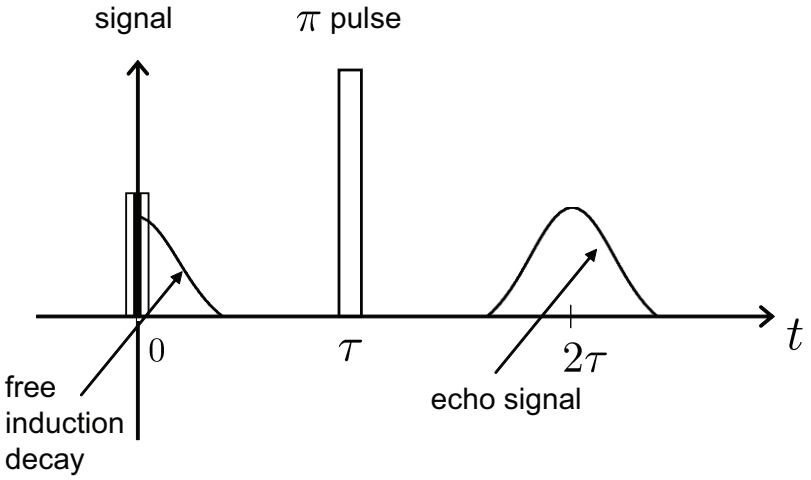

Figure 15.5: A free induction decay signal and spin echo signal.

$$\begin{aligned} \hat{X}^{-1}(\pi)\hat{I}_y\hat{X}(\pi) &= -\hat{I}_y \\ \hat{X}^{-1}(\pi)\hat{I}_z\hat{X}(\pi) &= -\hat{I}_z \\ \hat{X}^{-1}(\pi)\hat{I}_x\hat{X}(\pi) &= \hat{I}_x \quad . \end{aligned} \tag{15.40}$$

Quantum average in the integral of (15.38) is now written as

$$\begin{aligned} \langle\psi(t)|\hat{I}_y|\psi(t)\rangle &= \langle\psi(0)|\hat{X}^{-1}\left(\frac{\pi}{2}\right)\hat{T}^{-1}(\tau,h_0)\,\hat{X}^{-1}(\pi)\hat{T}^{-1}(t-\tau,h_0)\,\hat{I}_y \\ &\quad \times\hat{T}(t-\tau,h_0)\,\hat{X}(\pi)\hat{T}(\tau,h_0)\,\hat{X}(\pi/2)|\psi(0)\rangle \quad . \end{aligned} \tag{15.41}$$

If we substitute $\hat{I}=\hat{X}(\pi)\hat{X}^{-1}(\pi)$ on both sides of $\hat{I}_y$ in the right hand side of (15.41) and use

$$\hat{X}^{-1}(\pi)\hat{I}_y\hat{X}(\pi) = -\hat{I}_y \quad , \tag{15.42}$$

$$\hat{X}^{-1}(\pi)\hat{T}(t-\tau,h_0)\,\hat{X}(\pi) = \hat{T}^{-1}(t-\tau,h_0) \quad , \tag{15.43}$$

we have

$$\begin{aligned} \langle\hat{I}_y\rangle &= -\int P(h_0)\,dh_0\langle\psi(0)|\hat{X}^{-1}(\pi/2)\hat{T}^{-1}(\tau,h_0)\,\hat{T}(t-\tau,h_0)\,\hat{I}_y \\ &\quad \times\hat{T}^{-1}(t-\tau,h_0)\,\hat{T}(\tau,h_0)\,\hat{X}(\pi/2)\,|\psi(0)\rangle \quad . \end{aligned} \tag{15.44}$$

At a specific time $t=2\tau, \hat{T}^{-1}(\tau,h_0)\,\hat{T}(t-\tau,h_0)$ becomes an identity operator $\hat{I}$ so that we finally obtain

$$\begin{aligned} \langle\hat{I}_y\rangle_{t=2\tau} &= -\int P(h_0)\,dh_0\langle\psi(0)|\hat{X}^{-1}(\pi/2)\,\hat{I}_y\hat{X}(\pi/2)|\psi(0)\rangle \\ &= -\langle\hat{I}_z\rangle_{t=0} \quad . \end{aligned} \tag{15.45}$$

This is a spin echo signal.

15.2.2 Carr-Purcell sequence

If a longitudinal magnetic-field has not only a spatially inhomogeneous broadening h_0 but dynamically fluctuates, the cancellation of the accumulated phases between the first free evolution time $[0, \tau]$ and the second free evolution time $[\tau, 2\tau]$ becomes imperfect. If the free evolution time τ increases, the Larmor frequency modulation faster than the characteristic frequency $\sim 1/\tau$ all contribute to the imperfect rephasing. In order to suppress such an effect, we can send the sequence of $\hat{X}(\pi)$ pulses so that the spins can be refocused repeatedly as shown in Fig. 15.6. One can directly obtain the decoherence time T_2 by the decay of the envelop of the echo signals.

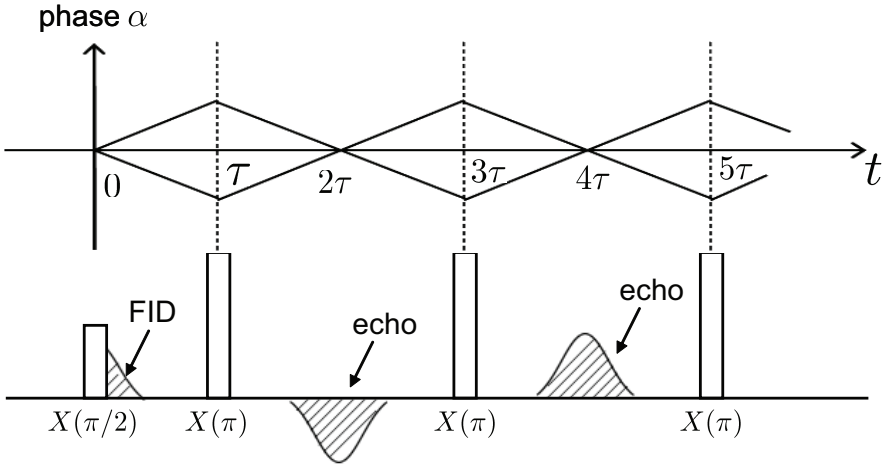

Figure 15.6: A Carr-Purcell sequence.

15.2.3 Meiboom-Gill sequence

If a $X(\pi)$ pulse area is not exactly equal to π, the phase error accumulates as the number of $X(\pi)$ pulses increases, as shown in Fig. 15.7.

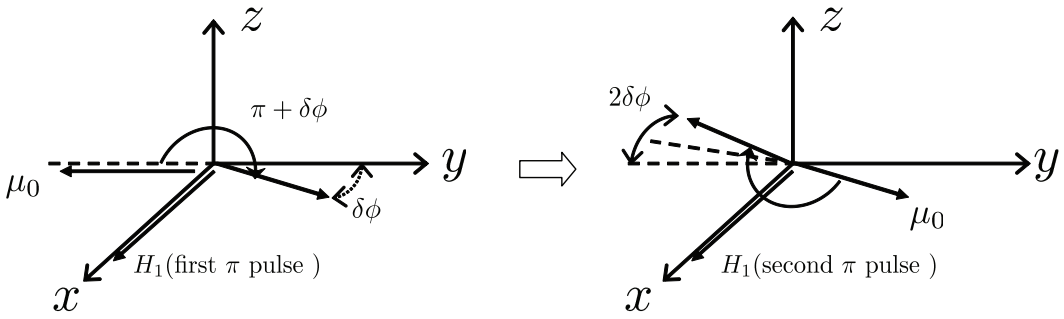

Figure 15.7: A phase error in the Carr-Purcell sequence.

One way to fix this problem is to change the phase of π pulses periodically such as

$$X\left(\frac{\pi}{2}\right) \quad \tau \quad X(\pi) \quad \tau \quad -X(\pi) \quad \tau \quad X(\pi)\cdots \quad . \tag{15.46}$$

The phase error introduced by $X(\pi)$ pulse is compensated for by the following $-X(\pi)$ pulse.

The other solution is

$$X\left(\frac{\pi}{2}\right) \quad \tau \quad Y(\pi) \quad \tau \quad -Y(\pi) \quad \tau \quad Y(\pi) \quad \tau \cdots \quad . \tag{15.47}$$

As shown in Fig. 15.8, the echo signals have the same polarity in this case.

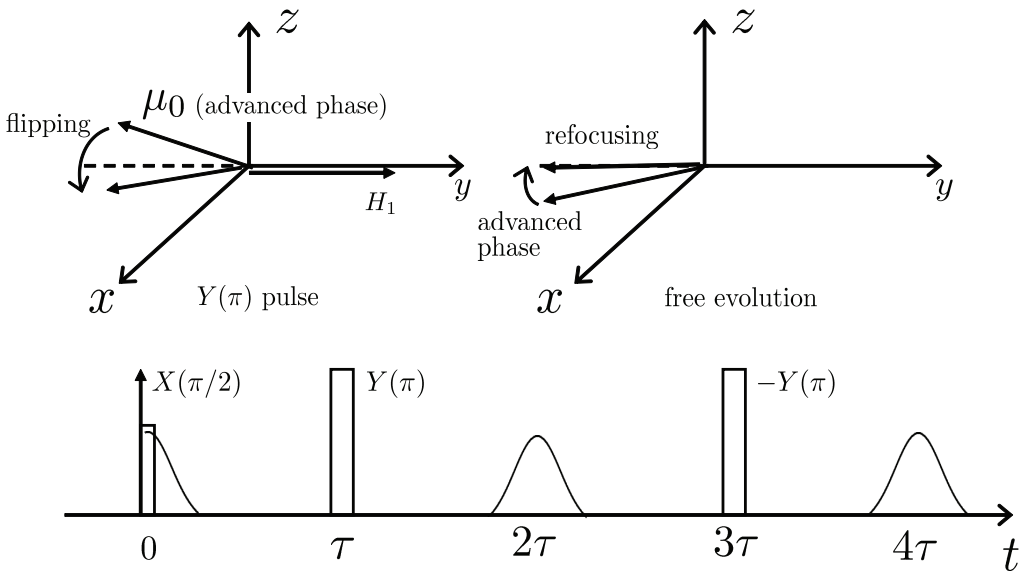

Figure 15.8: A Meiboom-Gill sequence.

15.3 Decoupling of spin qubits

15.3.1 Dipolar broadening of spin lattices

In an ensemble of identical spins, either electron spins or nuclear spins, forms a lattice structure, the magnetic coupling between such iso-spins is dominated by the dipolar Hamiltonian:

$$\hat{\mathcal{H}}_d = \frac{\gamma^2\hbar^2}{r^3}\hat{I}_{z1}\hat{I}_{z2}\left(1-3\cos^2\theta\right) \quad , \tag{15.48}$$

where we keep only leading term in the dipolar coupling. On the other hand, the Zeeman Hamiltonian is

$$\hat{\mathcal{H}}_z = -\gamma\hbar H_0\left(\hat{I}_{z1}+\hat{I}_{z2}\right) \quad , \tag{15.49}$$

where H_0 is a *dc* field. Comparison of (15.48) and (15.49) leads to the conclusion that the effect of spin 1 and spin 2 is understood as the local field created by spin 1 at a location of spin 2:

$$\hat{\mathcal{H}}_{loc} \simeq \frac{\gamma\hbar}{r^3}m_1 \quad , \tag{15.50}$$

where m_1 is either 1/2 (up-spin) or -1/2 (down-spin). If we substitute a nuclear gyromagnetic ratio γ_n for γ and a crystal lattice constant $a \sim 3\mathring{A}$ for r, the local field is on the order of $\sim 10^{-4}$ tesla. The line broadening $\Delta\omega$ due to the dipolar coupling from a surrounding spin bath is then of the order of

$$\frac{\Delta\omega}{\omega} = \frac{H_{loc}}{H_0} \simeq 10^{-4} \quad . \tag{15.51}$$

Here we assume the *dc* field is $H_0 = 1$ tesla. If a Larmor frequency ω at $H_0 = 1$ tesla is assumed to be $\frac{\omega}{2\pi} \sim 50$ MHz, the broadening of the line width is $\Delta\omega \sim 5$ KHz which corresponds to the dephasing time of $T_2^* \sim 200\mu$ sec. This is a big noise source for a nuclear spin system. If we substitute an electron gyromagnetic ratio γ_e for γ and electron spin separation $d \sim 300\mathring{A}$ for r, the local field is on the order of $\sim 10^{-7}$ tesla. If a Larmor frequency ω at $H_0 = 10$ tesla is assumed to be $\frac{\omega}{2\pi} \sim 50$ GHz, the broadening of the linewidth is $\Delta\omega \sim 0.5$ KHz which corresponds to the dephasing time of $T_2^* \sim 2$ msec. This is not a negligible effect for an electron spin system.

A dipolar coupling between iso-spins cannot be refocused by the spin echo (refocusing) techniques described in the previous section, because not only a specific spin (system) but all surrounding spins (bath) are simultaneously tipped by the refocusing pulses.

15.3.2 WAHUHA sequence

Since the dipolar coupling (15.48) is proportional to a factor $1 - 3\cos^2\theta$, where θ is the angle between the line connecting two spins and the spin polarization direction as shown in Fig. 15.9. Suppose we start with two spins polarized along z-axis and located on x-axis, as shown in Fig. 15.10, for which the angle θ is equal to $\frac{\pi}{2}$ according to the above definition. We then send a sequence of four $\pi/2$ pulses shown in Fig. 15.10. The average Hamiltonian over one period is then given by

$$\hat{\mathcal{H}}_{\text{eff}} = \frac{\gamma^2\hbar^2}{r^3}\hat{I}_{z1}\hat{I}_{z2} \cdot \frac{1}{6\tau}\left[1 \times 2\tau + 1 \times \tau - 2 \times 2\tau + 1 \times \tau\right] = 0 \quad . \tag{15.52}$$

We can eliminate the dipolar coupling approximately by such a pulse sequence. Repeated WAHUHA sequences can be sampled at an arbitary sampling time as shown in Fig. 15.11. This new WAHUHA can be combined with its mirror image to suppress an effect of angle errors introduced by imperfect pulse area. This sequence is called a MREV-8 pulse sequence.

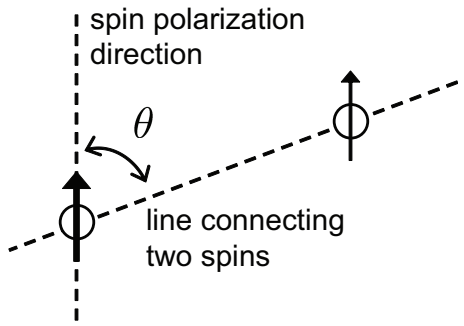

Figure 15.9: A dipolar coupling between two iso-spins.

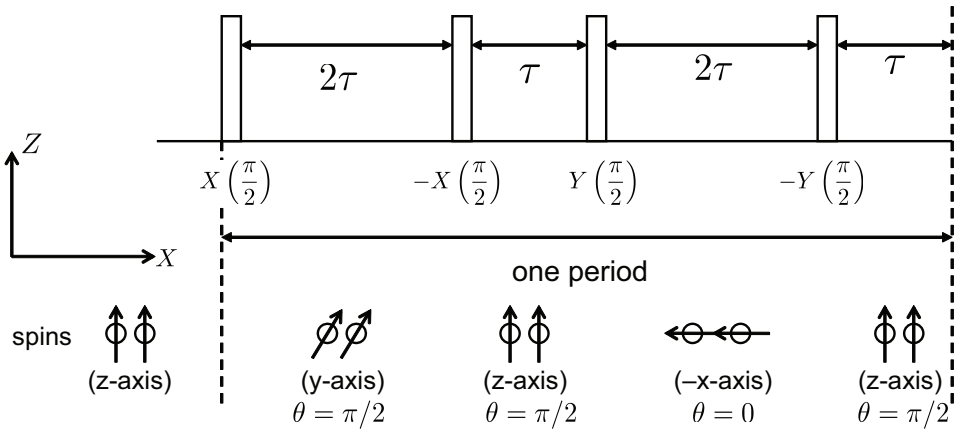

Figure 15.10: A WAHUHA pulse sequence.

15.3.3 Hadamard decoupling and selective recoupling [5]

If an ensemble of iso-spins can be distinguished individually by their locations, that is, by location-dependent Larmor frequency we can send the sequence of π pulses to eliminate the dipolar coupling. An example of four iso-spins is shown in Fig. 15.12. The spin orientation is modulated according to the Hadamard matrix, in which every raw vector is orthogonal to every other raw vector. After integration over one cycle, four spins can be then decoupled with each other. For arbitrary number of spins n, we can always use the over-sized Hadamard matrix to from one cycle, in which the dipolar coupling can be suppressed. One advantage of this decoupling scheme is that we can selectively recouple a particular pair of spins by introducing the same modulation pattern into these spins.

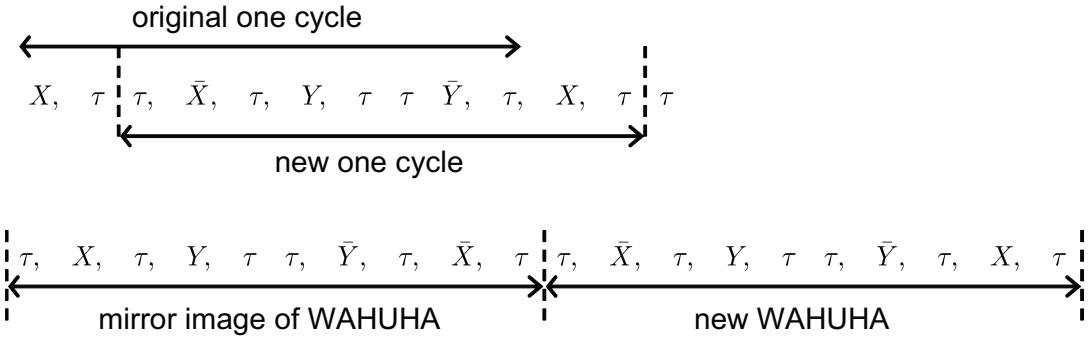

Figure 15.11: A MREV-8 pulse sequence.

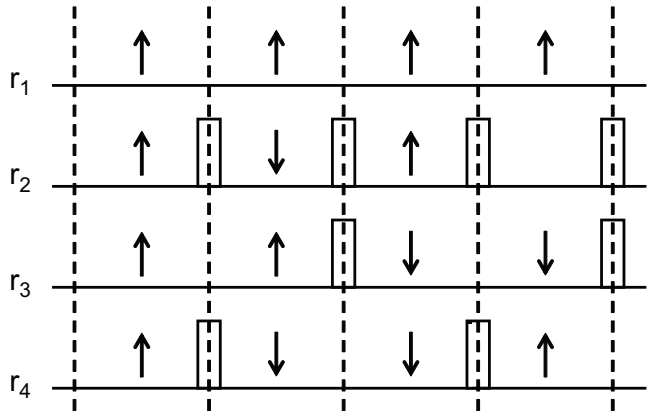

Figure 15.12: A Hadamard π pulse sequence.

15.4 Refocusing and decoupling experiments for electron spins and nuclear spins

D. Press et al., "Ultrafast Optical Spin Echo in a Single Quantum Dot, Nature Photonics 4, 367-370 (2010)

T. Ladd, D. Maryenko, Y. Yamamoto, E. Abe and K.M. Itoh, "Coherence time of decoupled nuclear spins in silicon, Phys. Rev. B 71, 014401 (January 2005).

Bibliography

[1] A. Abragam, Principles of Nuclear Magnetism *Clarendon Press, Oxford* (1961).

[2] M. Mehring, Principles of High Resolution NMR in Solids *Springer-Verlag, Berlin* (1983).

[3] V. Weisskopf and E. Wigner, *Z. Phys.* **63**, 54 (1930).

[4] E.L. Hahn, *Phys. Rev.* **80**, 580 (1950).

[5] D.W. Leung, I.L. Chuang, F. Yamaguchi and Y. Yamamoto, *Phys. Rev. A* **61**, 042310 (2000).

nature photonics

LETTERS

PUBLISHED ONLINE: 18 APRIL 2010 | DOI: 10.1038/NPHOTON.2010.83

Ultrafast optical spin echo in a single quantum dot

David Press[1]*, Kristiaan De Greve[1], Peter L. McMahon[1], Thaddeus D. Ladd[1,2]†, Benedikt Friess[1,3], Christian Schneider[3], Martin Kamp[3], Sven Höfling[3], Alfred Forchel[3] and Yoshihisa Yamamoto[1,2]

Many proposed photonic quantum networks rely on matter qubits to serve as memory elements[1,2]. The spin of a single electron confined in a semiconductor quantum dot forms a promising matter qubit that may be interfaced with a photonic network[3]. Ultrafast optical spin control allows gate operations to be performed on the spin within a picosecond timescale[4–14], orders of magnitude faster than microwave or electrical control[15,16]. One obstacle to storing quantum information in a single quantum dot spin is the apparent nanosecond-timescale dephasing due to slow variations in the background nuclear magnetic field[15–17]. Here we use an ultrafast, all-optical spin echo technique to increase the decoherence time of a single quantum dot electron spin from nanoseconds to several microseconds. The ratio of decoherence time to gate time exceeds 10^5, suggesting strong promise for future photonic quantum information processors[18] and repeater networks[1,2].

The preservation of the phase coherence of a qubit is essential for quantum computing and networking. The decoherence time is not a fundamental property of the qubit; rather it depends on how the qubit states are manipulated and measured. Although the intrinsic decoherence of an individual spin can be quite slow, electron spin coherence in an ensemble of quantum dots (QDs) is typically lost on a nanosecond timescale due to inhomogeneous broadening[19,20]. In a single, isolated QD, there is no inhomogeneous broadening due to ensemble averaging. However, when a single spin is measured repeatedly, it will suffer from temporally averaged dephasing if it evolves differently from one measurement to the next. In an InAs QD, the hyperfine interaction of an electron with nuclear spins causes a slowly fluctuating background magnetic field, which leads to a short dephasing time T_2^* on the order of 1–10 ns after temporal averaging[15–17]. This dephasing can be largely reversed using a spin echo[8,12,15,16,21], which rejects low-frequency nuclear-field noise by refocusing the phase of the spin, as demonstrated using microwave and electrical techniques in electrically gated (optically inactive) QDs[15,16]. The spin-echo technique allows a qubit of information to be stored throughout the spin's decoherence time T_2, which is limited by dynamical processes such as nuclear spin diffusion and electron-nuclear spin feedback[22–25].

The decoherence time T_2 of an ensemble of QDs has been measured to be ~3 μs using a train of ultrafast optical pulses in a 'spin-locking' technique[7], a method that does not allow quantum information to be actively stored and manipulated in individual spins. On the other hand, spin refocusing techniques such as the Hahn spin-echo sequence ($(\pi/2)-\pi-(\pi/2)$ rotations) do allow direct manipulation and storage of a single qubit of information.

Our qubit is formed by the spin of a single electron confined within an InAs QD. A strong external magnetic field B_{ext} is applied perpendicular to the optical axis (Voigt geometry, see Fig. 1a) to split the spin eigenstates $|\downarrow\rangle$ and $|\uparrow\rangle$ by a Larmor frequency $\delta_e = g_e\mu_B B_{ext}/h$ of a few tens of gigahertz. Each of the metastable ground states $|\downarrow\rangle$ and $|\uparrow\rangle$ may be optically coupled to two charged-exciton states, denoted $|\downarrow\uparrow, \Downarrow\rangle$ and $|\downarrow\uparrow,\Uparrow\rangle$, which each contain two electrons in a spin-singlet and an unpaired heavy hole. To manipulate the electron spin state, we apply to the QD a circularly polarized, broadband optical pulse from a mode-locked laser. The pulse coherently rotates the spin between $|\downarrow\rangle$ and $|\uparrow\rangle$ by a stimulated Raman transition with an effective Rabi frequency Ω_{eff} (ref. 10).

Before a sequence of rotation pulses is applied, the spin state is first initialized into the ground state $|\uparrow\rangle$ by optical pumping[26]. A ~26-ns pulse is generated from a continuous-wave laser that drives the $|\downarrow\rangle \leftrightarrow |\downarrow\uparrow, \Downarrow\rangle$ transition with rate Ω_p. Spontaneous decay at a rate of $\Gamma/2$ from $|\downarrow\uparrow, \Downarrow\rangle$ initializes the spin into $|\uparrow\rangle$ within a few nanoseconds[10,27]. After application of the sequence of rotation pulses, the spin-state is measured by the next optical pumping pulse. If the spin was flipped to $|\downarrow\rangle$ by the rotation sequence, then the QD will emit a single photon from the $|\downarrow\uparrow, \Downarrow\rangle \rightarrow |\uparrow\rangle$ transition as the spin is re-initialized. This photon is spectrally filtered and detected using a single-photon counter.

Rabi oscillations between the two spin states $|\downarrow\rangle$ and $|\uparrow\rangle$ are shown in Fig. 1c as the intensity of a single rotation pulse is varied. The height of the first Rabi oscillation is lower than that of the second because of Larmor precession during the rotation pulse, which causes the Bloch vector to rotate off-axis for small rotation angles[10]. The Rabi oscillations are significantly less damped than in previous work[10] due to sample improvements and a smaller red-detuning of the rotation laser frequency relative to the QD transition frequency. As the time offset between a pair of $\pi/2$ rotation pulses is varied in Fig. 1d, Ramsey interference fringes show improved contrast compared to those in ref. 10 because the optical pump is gated off during spin precession.

A spin-echo pulse sequence consists of a first $\pi/2$ rotation to generate a coherence between the $|\uparrow\rangle$ and $|\downarrow\rangle$ states, followed by a time delay T during which the spin dephases freely. Next, a π rotation is applied, which effectively reverses the direction of the spin's dephasing. The spin rephases during another time delay T, at which point another $\pi/2$ rotation is applied to read out the coherence of the spin.

The photon count rate following a spin-echo pulse sequence as the time offset τ is varied is shown in Fig. 2a, for a total delay time of $2T = 264$ ns at a magnetic field of $B_{ext} = 4$ T. For short time offsets, coherent sinusoidal fringes are observed. Because our experimental apparatus lengthens the first time delay by τ while simultaneously shortening the second delay by τ, we observe the spin-echo signal oscillating at twice the Larmor frequency: $\cos[2\pi\delta_e(2\tau)]$. For longer time offsets, however, T_2^* dephasing becomes apparent as the phase of the fringes becomes incoherent

[1]E. L. Ginzton Laboratory, Stanford University, Stanford, California 94305, USA, [2]National Institute of Informatics, Hitotsubashi 2-1-2, Chiyoda-ku, Tokyo 101-8403, Japan, [3]Technische Physik, Physikalisches Institut, Wilhelm Conrad Röntgen Research Center for Complex Material Systems, Universität Würzburg, Am Hubland, D-97074 Würzburg, Germany; †Present address: HRL Laboratories, LLC, 3011 Malibu Canyon Road, Malibu, California 90265, USA. *e-mail: dlpress@stanford.edu

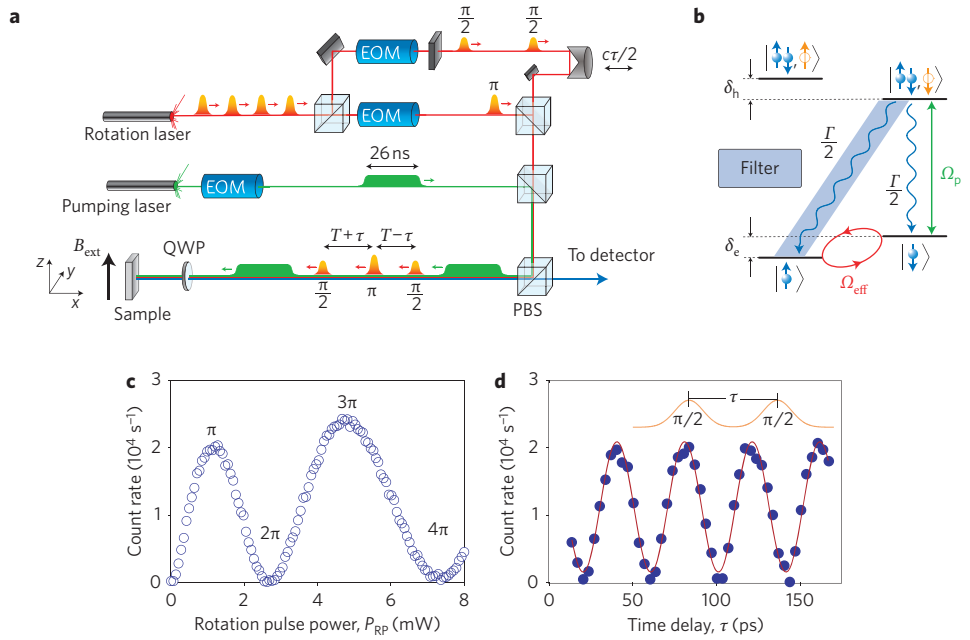

Figure 1 | Experimental set-up for optical single-spin manipulation and detection. a, Experimental set-up. One arm of the rotation laser path generates $\pi/2$ pulses, and the other arm generates π pulses. QWP, quarterwave plate; PBS, polarizing beamsplitter; EOM, electro-optic modulator. **b**, Energy level diagram. **c**, Rabi oscillations between the two spin states lead to a count rate that oscillates with varied rotation laser power P_{RP}. **d**, Ramsey interference fringes as the time offset between two $\pi/2$ rotation pulses is varied.

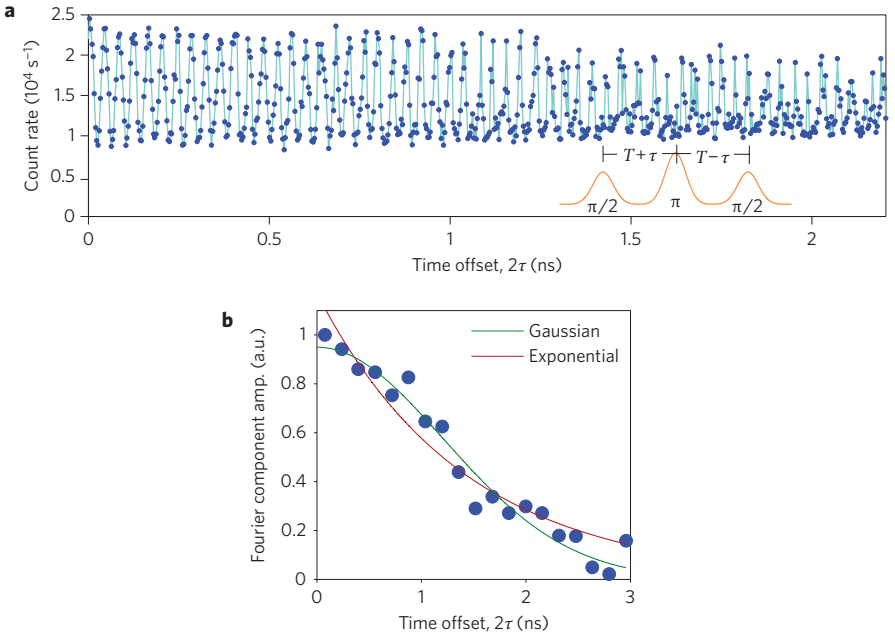

Figure 2 | Experimental demonstration of spin echo and single-spin dephasing. a, Spin-echo signal as the time offset 2τ is varied, for a time delay of $2T = 264$ ns and magnetic field $B_{ext} = 4$ T. Single-spin dephasing is evident at large time offset. **b**, Decaying Fourier component of fringes. Red line, exponential fit; green line, Gaussian fit. The one-standard-deviation confidence interval described in the text is determined by bootstrapping.

and random due to the background nuclear field fluctuating between one measurement and the next. Note that this behaviour is different from that observed when averaging over a spatial ensemble of spins or using long time-averaging: in these cases, the data would resemble a damped sinusoid with decaying amplitude but well-defined phase[19]. The directly observed phase randomization suggests that the timescale of the fluctuation of the nuclear field is longer than our measurement time per data point (~2 s).

To quantify the dephasing time T_2^*, we performed a running Fourier transform on blocks of the data four Larmor periods in length; the amplitude of the appropriate Fourier component is plotted in Fig. 2b. The data are slightly better fit by a Gaussian decay (green line, $\exp(-t^2/T_2^{*2})$), than a single exponential (red line, $\exp(-t/T_2^*)$), which is consistent with dephasing induced by random nuclear magnetization. For the Gaussian fit, we find $T_2^* = 1.71 \pm 0.08$ ns.

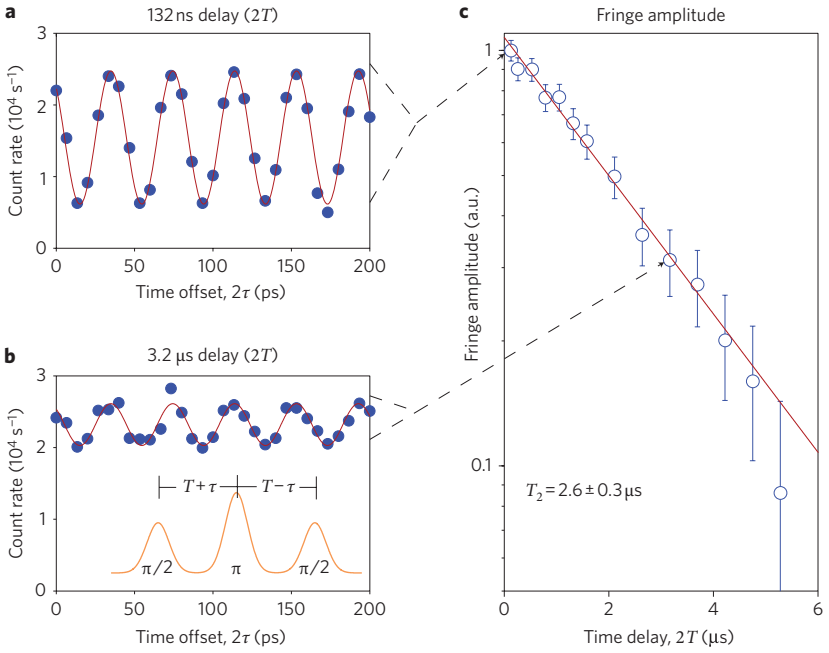

Figure 3 | Measurement of T_2 using spin echo. a, Spin-echo signal as the time offset 2τ is varied, for a time delay of $2T = 132$ ns. Magnetic field $B_{ext} = 4$ T. **b**, Spin-echo signal for a time delay of $2T = 3.2$ μs. **c**, Spin-echo fringe amplitude on a semilog plot versus time delay $2T$, showing a fit to an exponential decay. Error bars represent one-standard-deviation confidence intervals estimated by taking multiple measurements of the same delay curve.

To investigate T_2 decoherence, we varied the time delay T of the spin-echo sequence and observed the coherent fringes for small time offset $\tau \ll T_2^*$. The count rate as a function of time offset 2τ, at a magnetic field of $B_{ext} = 4$ T and an echo time delay of $2T = 132$ ns, is shown in Fig. 3a. The data for such small time offsets τ are well fit by a sinusoid. Figure 3b shows that the amplitude of the spin-echo fringes for a delay time of $2T = 3.2$ μs is much smaller compared to that for $2T = 132$ ns. The spin-echo fringe amplitude versus total time $2T$ is shown in Fig. 3c, and is well fit by a single exponential decay with decoherence time $T_2 = 2.6 \pm 0.3$ μs. This decoherence time is in close agreement with that measured for an ensemble of QD electron spins by optical spin-locking at a high magnetic field[7].

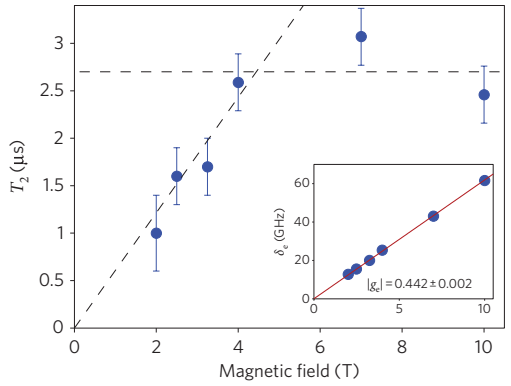

Figure 4 | Magnetic field dependence of T_2. Decoherence time T_2 at various magnetic fields B_{ext}. Error bars represent one-standard-deviation confidence intervals estimated from three independent measurements of the $B_{ext} = 4$ T experiment, combined with bootstrapped uncertainties from each coherence decay curve. Black dashed lines are guides to the eye that indicate an initial rising slope, and then saturation for high magnetic fields. The inset shows the linear dependence of the Larmor precession frequency δ_e on the magnetic field. The slope uncertainty is determined by bootstrapping.

The decoherence time T_2 is plotted as a function of magnetic field B_{ext} in Fig. 4. The coherence decay curves over a wide range of magnetic fields were well fit by single exponentials, but sizable error bars prevent us from conclusively excluding other decay profiles. The data show that T_2 increases with magnetic field at low fields $B_{ext} < 4$ T. T_2 seems to saturate at high magnetic field. Theory predicts that decoherence should be dominated by magnetic field fluctuations caused by random inhomogeneities of the nuclear magnetization inside the QD diffusing via the field-independent nuclear dipole–dipole interaction. Higher-order processes such as hyperfine-mediated nuclear spin interactions are not expected for spin echo at these magnetic fields[24]. Consequently, the spin-echo decoherence time is predicted to be invariant with magnetic field, and to be in the range 1–6 μs for an InAs QD of our dimensions[23–25]. Our high-field results of $T_2 \approx 3$ μs for $B_{ext} \gtrsim 4$ T are consistent with these predictions, and also consistent with experimental results measured by spin-locking[7]. For low fields, T_2 may be limited by spin fluctuations in paramagnetic impurity states close to the QD, the spin states of which become frozen out at high fields. Our observation of shorter T_2 times for QDs close to etched surface interfaces (see Methods) is also consistent with this picture. The inset to Fig. 4 shows that the Larmor precession frequency δ_e increases linearly with magnetic field B_{ext} as expected, with a slope corresponding to an electron g-factor $|g_e| = 0.442 \pm 0.002$. Using our optical manipulation techniques, an arbitrary single-qubit gate operation may be completed within one Larmor precession period: $T_{gate} = 1/\delta_e$ (ref. 10). At the highest magnetic field of 10 T, the ratio of decoherence time to gate time is $T_2/T_{gate} = 150{,}000$.

In conclusion, we have implemented a several-microsecond quantum memory in a single-QD electron spin. By applying an ultrafast optical spin-echo sequence, we reversed the rapid dephasing caused by a slowly varying background nuclear field, and extended the decoherence time from nanoseconds to microseconds. As the applied magnetic field is increased, the decoherence time first increases, and then saturates at ~3 μs for high fields. This decoherence time exceeds the single-qubit gate operation time by more than

five orders of magnitude. This work represents an ultrafast, all-optical implementation of a vital technique from magnetic resonance, and demonstrates the strong potential for QD–spin qubits to form the building blocks of photonic quantum logic devices and networks.

Methods

The sample contained $\sim 2 \times 10^9$ cm^{-2} self-assembled InAs QDs grown by the Stranski-Krastanow method at the centre of a planar GaAs microcavity. The QDs were ~30 nm in diameter. A δ-doping layer of $\sim 1 \times 10^{10}$ cm^{-2} silicon donors was grown 10 nm below the QD layer to probabilistically charge the QDs. Approximately one-third of the QDs were charged, and these could be identified by their splitting into symmetrical quadruplets at high magnetic fields[28]. The lower and upper cavity mirrors contained 24 and 5 pairs of $Al_{0.9}Ga_{0.1}As/GaAs$ $\lambda/4$ layers, respectively, giving the cavity a quality factor of ~200. The cavity increased the signal-to-noise ratio of the measurement in two ways. First, it increased the collection efficiency by directing most of the QD emission towards the objective lens and, second, it reduced the laser power required to achieve optical pumping, thereby reducing the reflected pump-laser noise. The planar microcavity was capped with a 100-nm-thick aluminium mask with 10-μm windows for optical access. There were on the order of 10 QDs within the ~1-μm-diameter excitation spot, and at most one of these QDs was resonant with the cavity at an emission wavelength of ~940 nm.

The sample presented in this work represents the third generation of our electron spin QD samples. The first generation contained δ-doped InAs QDs in 600-nm-diameter mesa structures[10]. The spin-echo decoherence time T_2 was ~70 ns, which we attributed to charge fluctuations of surface states on the etched mesa sidewalls. The second-generation sample contained δ-doped InAs QDs in 2-μm-diameter single-sided pillar microcavities with SiN surface passivation. T_2 was increased to ~600 ns, probably because passivation reduced the number of surface states. The third-generation metal-masked planar samples used in this work were designed to eliminate all etched surfaces near the QDs.

The sample was cooled to 1.5 K in a superconducting magnetic cryostat with a variable magnetic field up to 10 T. An aspheric objective lens with NA = 0.68 was placed inside the cryostat to focus both pump and rotation lasers onto the sample. The sample was positioned inside the cryostat using piezo-electric 'slip-stick' positioners. Single-photon photoluminescence was collected through the same lens and directed onto a single-photon counter. The QD emission was spectrally filtered using a double-monochromator with a resolution of 0.02 nm. Scattered laser light was further rejected by double-passing through a quarterwave plate and polarizer. The 4-ps duration pulses of the rotation laser were detuned by ~150 GHz below the lowest transition. The rotation laser path was divided into two arms: one arm generated $\pi/2$ rotations and the other generated π rotations. A pair of free-space electro-optic modulators (EOMs) were used as pulse-pickers to generate a sequence of three rotation pulses separated by an integer multiple of mode-locked laser repetition periods $T = nT_r$, where $T_r = 13.2$ ns. Each EOM was double-passed to achieve extinction ratios of $\sim 10^4$. A computer-controlled stage allowed a fine time offset τ between the $\pi/2$ and π rotations. The optical pumping laser was gated by a fibre-based EOM with an extinction ratio of $\sim 10^4$ into ~26-ns pulses.

All EOMs were controlled by a data pattern generator synchronized to the mode-locked rotation laser. The rotation laser was chopped at 1 kHz by electronically gating the EOMs, and the single-photon counts were detected by a digital lock-in counter synchronized to this frequency. To reject detector dark counts during the precession period of the spin, the photon counters were gated on only during the 26-ns optical pumping pulse.

Received 29 November 2009; accepted 5 March 2010; published online 18 April 2010

References

1. Cirac, J. I., Zoller, P., Kimble, H. J. & Mabuchi, H. Quantum state transfer and entanglement distribution among distant nodes in a quantum network. *Phys. Rev. Lett.* **78,** 3221–3224 (1997).
2. Duan, L.-M., Lukin, M. D., Cirac, J. I. & Zoller, P. Long-distance quantum communication with atomic ensembles and linear optics. *Nature* **414,** 413–418 (2001).
3. Yao, W., Liu, R.-B. & Sham, L. J. Theory of control of the spin-photon interface for quantum networks. *Phys. Rev. Lett.* **95,** 030504 (2005).
4. Gupta, J. A., Knobel, R., Samarth, N. & Awschalom, D. D. Ultrafast manipulation of electron spin coherence. *Science* **292,** 2458–2461 (2001).
5. Berezovsky, J., Mikkelson, M. H., Stoltz, N. G., Coldren, L. A. & Awschalom, D. D. Picosecond coherent optical manipulation of a single electron spin in a quantum dot. *Science* **320,** 349–352 (2008).
6. Dutt, M. V. G. *et al.* Ultrafast optical control of electron spin coherence in charged GaAs quantum dots. *Phys. Rev. B* **74,** 125306 (2006).
7. Greilich, A. *et al.* Mode locking of electron spin coherences in singly charged quantum dots. *Science* **313,** 341–345 (2006).
8. Greilich, A. *et al.* Ultrafast optical rotations of electron spins in quantum dots. *Nature Phys.* **5,** 262–266 (2007).
9. Carter, S. G., Chen, Z. & Cundiff, S. T. Ultrafast below-resonance Raman rotation of electron spins in GaAs quantum wells. *Phys. Rev. B* **76,** 201308(R) (2007).
10. Press, D., Ladd, T. D., Zhang, B. & Yamamoto, Y. Complete quantum control of a single quantum dot spin using ultrafast optical pulses. *Nature* **456,** 218–221 (2008).
11. Carter, S. G. *et al.* Directing nuclear spin flips in InAs quantum dots using detuned optical pulse trains. *Phys. Rev. Lett.* **102,** 167403 (2009).
12. Clark, S. *et al.* Ultrafast optical spin echo for electron spins in semiconductors. *Phys. Rev. Lett.* **102,** 247601 (2009).
13. Phelps, C., Sweeney, T., Cox, R. T. & Wang, H. Ultrafast coherent electron spin flip in a modulation-doped CdTe quantum well. *Phys. Rev. Lett.* **102,** 237402 (2009).
14. Kim, E. D. *et al.* Fast spin rotations and optically controlled geometric phases in a quantum dot. Preprint at <http://arXiv.org/0910.5189> (2009).
15. Petta, J. R. *et al.* Coherent manipulation of coupled electron spins in semiconductor quantum dots. *Science* **309,** 2180–2184 (2005).
16. Koppens, F. H. L., Nowack, K. C. & Vandersypen, L. M. K. Spin echo of a single electron spin in a quantum dot. *Phys. Rev. Lett.* **100,** 236802 (2008).
17. Xu, X. *et al.* Optically controlled locking of the nuclear field via coherent dark-state spectroscopy. *Nature* **459,** 1105–1109 (2009).
18. Imamoğlu, A. *et al.* Quantum information processing using quantum dot spins and cavity QED. *Phys. Rev. Lett.* **83,** 4204–4207 (1999).
19. Dutt, M. V. G. *et al.* Stimulated and spontaneous optical generation of electron spin coherence in charged GaAs quantum dots. *Phys. Rev. Lett.* **94,** 227403 (2005).
20. Bracker, A. S. *et al.* Optical pumping of the electronic and nuclear spin of single charge-tunable quantum dots. *Phys. Rev. Lett.* **94,** 047402 (2005).
21. Hahn, E. L. Spin echoes. *Phys. Rev.* **80,** 580–594 (1950).
22. Coish, W. A. & Loss, D. Hyperfine interaction in a quantum dot: non-Markovian electron spin dynamics. *Phys. Rev. B* **70,** 195340 (2004).
23. Witzel, W. M. & Das Sarma, S. Quantum theory for electron spin decoherence induced by nuclear spin dynamics in semiconductor quantum computer architectures: spectral diffusion of localized electron spins in the nuclear solid-state environment. *Phys. Rev. B* **74,** 035322 (2006).
24. Yao, W., Liu, R.-B. & Sham, L. J. Theory of electron spin decoherence by interacting nuclear spins in a quantum dot. *Phys. Rev. B* **74,** 195301 (2006).
25. Liu, R.-B., Yao, W. & Sham, L. J. Control of electron spin decoherence caused by electron-nuclear spin dynamics in a quantum dot. *New J. Phys.* **9,** 226 (2007).
26. Atatüre, M. *et al.* Quantum-dot spin-state preparation with near-unity fidelity. *Science* **312,** 551–553 (2006).
27. Xu, X. *et al.* Fast spin state initialization in a singly charged InAs–GaAs quantum dot by optical cooling. *Phys. Rev. Lett.* **99,** 097401 (2007).
28. Bayer, M. *et al.* Fine structure of neutral and charged excitons in self-assembled In(Ga)As/(Al)GaAs quantum dots. *Phys. Rev. B* **65,** 195315 (2002).

Acknowledgements

This work was supported by the National Institute of Information and Communications Technology (NICT Japan), the Ministry of Education, Culture, Sports, Science and Technology (MEXT Japan), the National Science Foundation (CCF0829694), the National Institute of Standards and Technology (60NANB9D9170), the Special Coordination Funds for Promoting Science and Technology and the State of Bavaria. We thank T. Steinl, A. Wolf and M. Emmerling for their assistance with sample fabrication. P.L.M. was supported by a David Cheriton Stanford Graduate Fellowship.

Author contributions

C.S., M.K., and S.H. grew and fabricated the sample. D.P., K.D.G. and P.L.M. carried out the optical experiments. B.F. wrote the data acquisition software. T.D.L. provided theoretical analysis and guidance. Y.Y. and A.F. guided the work. D.P. wrote the manuscript with input from all authors.

Additional information

The authors declare no competing financial interests. Reprints and permission information is available online at http://npg.nature.com/reprintsandpermissions/. Correspondence and requests for materials should be addressed to D.P.

Coherence time of decoupled nuclear spins in silicon

T. D. Ladd,* D. Maryenko,† and Y. Yamamoto‡
Quantum Entanglement Project, SORST, JST, Edward L. Ginzton Laboratory, Stanford University, Stanford, California 94305-4085, USA

E. Abe and K. M. Itoh
Department of Applied Physics and Physico-Informatics, CREST, JST, Keio University, Yokohama, 223-8522, Japan
(Received 18 August 2004; published 4 January 2005)

We report NMR experiments using high-power rf decoupling techniques to show that a ^{29}Si nuclear spin in a solid silicon crystal at room temperature can preserve quantum phase for 10^9 precessional periods. The coherence times we report are more than four orders of magnitude longer than for any other observed solid-state qubit. We also examine coherence times using magic-angle-spinning techniques and in isotopically altered samples. In high-quality crystals, coherence times are limited by residual dipolar couplings and can be further improved by isotopic depletion. In defect-heavy samples, we provide evidence for decoherence limited by a noise process unrelated to the dipolar coupling. The nonexponential character of these data is compared to a theoretical model for decoherence due to the same charge trapping mechanisms responsible for $1/f$ noise. These results provide insight into proposals for solid-state nuclear-spin-based quantum memories and quantum computers based on silicon.

DOI: 10.1103/PhysRevB.71.014401 PACS number(s): 82.56.Jn, 03.67.Lx, 03.67.Pp, 76.60.Lz

I. INTRODUCTION

Quantum information processing devices outperform their classical counterparts by preserving and exploiting the correlated phases of their constituent quantum oscillators, which are usually two-state systems called "qubits." An increasing number of theoretical proposals have shown that such devices allow secure long-distance communication and improved computational power.[1] Solid-state implementations of these devices are favored due to both scalability and ease of integration with existing hardware, although previous experiments have shown limited coherence times for solid-state qubits. The development of quantum error-correcting codes[2] and fault-tolerant quantum computation[3] showed that large-scale quantum algorithms are still theoretically possible in the presence of decoherence. However, the coherence time must be dauntingly long: approximately 10^5 times the duration of a single quantum gate, and probably longer depending on the quantum computer architecture.[1] The question of whether a scalable implementation can surpass this coherence threshold is not only important for the technological future of quantum computation, but also for fundamental understanding of the border between microscopic quantum behavior and macroscopic classical behavior.

Nuclear spins have long been considered strong candidates for robust qubits.[4,5] In particular, the magnetic moment of a spin-1/2 nucleus intrinsically possesses the qubit's simple two-state structure and has no direct coupling to local electric fields, making it extremely well isolated from the environment. The ^{29}Si isotope in semiconducting silicon is one example of such an isolated nucleus. Even at room temperature, the rate of thermal equilibrium for a ^{29}Si nuclear spin (T_1) exceeds 4 h, with much longer rates as the temperature is lowered.[6] When this T_1 time scale is compared to the resonant frequencies for such nuclei at even modest magnetic fields, it is clear that these nuclei are extremely weakly coupled to any external degrees of freedom. Due to this isolation, combined with the highly developed engineering surrounding silicon, both the ^{29}Si nucleus and the ^{31}P impurity nucleus in silicon have been proposed as qubits in architectures for quantum computing.[7,8]

The important time scale for quantum information is not the rate at which *energy* is exchanged with the environment, T_1, but rather the rate at which *information* is exchanged, a rate which manifests as the loss of phase coherence, T_2. The low resonant energy has led to speculation that T_2 for isolated nuclei in silicon will be similar to T_1. Such speculation has not been tested because *isolated* nuclei are not available for measurement; the low sensitivity of nuclear detection has, in all experiments to date, required a large ensemble of nuclei, and these ensemble members couple to each other via magnetic dipolar couplings much more strongly than they couple to the environment. Existing measurements of T_2 for silicon nuclei therefore measure only the dynamics of these dipole couplings, albeit modified by the spin-echo pulse sequences intended to eliminate inhomogeneous broadening.[9]

In the present study, we attempt to determine the coherence of isolated ^{29}Si nuclei, principally by applying well-known rf pulse sequences and sample-spinning techniques which serve to reverse dipolar dynamics. These pulse sequences slow down dipolar evolution by over three orders of magnitude. We also use these methods while varying the isotopic content of ^{29}Si among the spin-0 ^{28}Si and ^{30}Si isotopes.[10] These decoupling techniques and isotopic modifications, discussed in Sec. II, will both be necessary in quantum computer architectures.[7,8,11]

In very pure single-crystal samples, which are expected to have the longest values of T_2, we extend the decoherence time to 25 s, limited by internuclear dipolar couplings left over by the imperfect decoupling techniques. In defect-heavy silicon samples, however, we are able to decouple nuclei

well enough to observe intrinsic, lattice-induced decoherence. We find that low-frequency electronic fluctuations limit T_2 to still be much shorter than T_1 in these samples. These results are discussed in Sec. III. In Sec. IV, we discuss the processes which limit T_2 in our experiments. In particular we argue that the nonexponential decoherence we observe in polycrystalline silicon can be explained using a well-known model for electronic $1/f$ noise. To our knowledge, this is the first observation of such decoherence in solid-state NMR.

II. METHODS

In this work, we use the term "coherence" to refer to the coherence of single nuclei. In all experiments, we begin by placing many nuclei in the equal superposition state

$$|\psi\rangle = \frac{1}{\sqrt{2}}(|\uparrow\rangle + e^{i\phi}|\downarrow\rangle), \tag{1}$$

and we seek to learn how the phase ϕ shifts in time between different nuclei. This dephasing is revealed by an *ensemble* measurement; if inhomogeneous broadening is eliminated, the ensemble result is similar to measuring a single nucleus repeatedly and averaging the results. Differences between ensemble and single-spin measurements are discussed in Appendix A. This single-spin definition of coherence is not always appropriate in solid-state NMR because nuclei evolve under dipolar couplings into coherent, highly correlated, many-body states. These states may be observed in experiments designed to measure "multiple quantum coherences;"[12] such experiments show that even when the phase information of single nuclei has become lost to the ensemble, the ensemble as a whole has not lost that information to the environment. However, in the present study, as in ensemble-based quantum computers,[5,7] we regard the evolution of such intraensemble correlations as a decoherence process, but one which we are able to partially reverse. We present the Hamiltonian governing the spin system in Sec. II A, and we summarize the theory behind the methods for partially reversing the dipolar coupling in Sec. II B. The specific challenges for experimental application of these methods to silicon are discussed in Sec. II C.

A. The spin system

The largest term in the nuclear Hamiltonian is the Zeeman term,

$$\mathcal{H}_Z = -\hbar\gamma B_0 \sum_j I_j^z - \hbar\gamma \sum_j \delta\mathbf{B}(\mathbf{r}_j)\cdot\mathbf{I}_j, \tag{2}$$

where $\mathbf{I}_j$ is the spin operator for the jth ^{29}Si nucleus and $\delta\mathbf{B}(\mathbf{r}_j)$ is the static deviation of the local magnetic field from the applied field $B_0\hat{\mathbf{z}}$ at the position $\mathbf{r}_j$ of the jth nucleus. It is convenient to shift to the "rotating reference frame,"[13] both because the uninteresting fast z rotation is removed, and because heterodyne inductive measurement effectively observes dynamics in this frame. This frame rotates about the z axis at the frequency $\omega \approx \gamma B_0$ of the applied radio-frequency (rf) field. Neglecting terms which oscillate at ω (rotating wave approximation), the Zeeman term is rewritten

$$\mathcal{H}_0 = -\hbar\sum_j \omega_j I_j^z, \tag{3}$$

where $\omega_j = \gamma[B_0 + \delta B^z(\mathbf{r}_j)] - \omega$. This unperturbed Hamiltonian sets the resonant frequency for each nucleus; completely "coherent" nuclei would evolve according to this term alone. Note that dephasing would still occur in the ensemble due to the variation of ω_j between nuclei (i.e., due to inhomogeneous magnetic fields); this dephasing is readily refocused as a spin echo and is therefore not regarded as decoherence.

The dipolar coupling, also in the rotating wave approximation, is written[13]

$$\mathcal{H}_D = -\sum_{j\neq k} D_{jk}[\mathbf{I}_j\cdot\mathbf{I}_k - 3I_j^z I_k^z]. \tag{4}$$

The dipolar coupling coefficients are

$$D_{jk} = \hbar^2\gamma^2\frac{1-3\cos^2\theta_{jk}}{r_{jk}^3}, \tag{5}$$

where $r_{jk}\cos\theta_{jk} = (\mathbf{r}_j - \mathbf{r}_k)\cdot\hat{\mathbf{z}}$. For silicon sparse in the ^{29}Si isotope, as is isotopically natural silicon, the ^{29}Si nuclei are randomly located in the crystal lattice, leading to a random distribution of coupling constants D_{jk}.

Most solid-state NMR experiments are completely described by the "internal" Hamiltonian $\mathcal{H}_{int} = \mathcal{H}_0 + \mathcal{H}_D$, along with the collective rotations controlled by rf fields, *except* for the presence of T_1 relaxation, which requires a term coupling the nuclear spin system to local fluctuating magnetic fields. In the present work, we shall also be concerned with T_2 decoherence due to such local fields. We therefore suppose the presence of a semiclassical random field $\mathbf{b}(\mathbf{r},t)$ leading to the term

$$\mathcal{H}_{env}(t) = -\hbar\gamma\sum_j \mathbf{b}(\mathbf{r}_j,t)\cdot\mathbf{I}_j(t). \tag{6}$$

For the present work at room temperature, there is no reason to treat the decohering environment in a quantum mechanical way. The consequences of this term and the statistics of the random field $\mathbf{b}(\mathbf{r},t)$ will be discussed in Sec. IV B.

B. Theory of dipolar decoupling

The dipolar evolution, as governed by Eq. (4), is the principal bottleneck for resolution in solid-state NMR spectroscopy. As a result, a variety of techniques have been developed to periodically reverse that evolution; we refer to such techniques as "decoupling." Discussion of these techniques can be found in standard NMR textbooks.[14] In this section, we review only the pertinent details required to understand the present results. We begin by discussing multiple pulse sequences (MPSs) for decoupling, and the related technique of magic angle spinning (MAS).

1. Multiple pulse sequences

In MPS decoupling, rapid rotations are applied to the spin system by short rf pulses in a periodic cycle. The key concept for comprehension of MPS decoupling is the toggling reference frame. This reference frame "follows" the pulses;

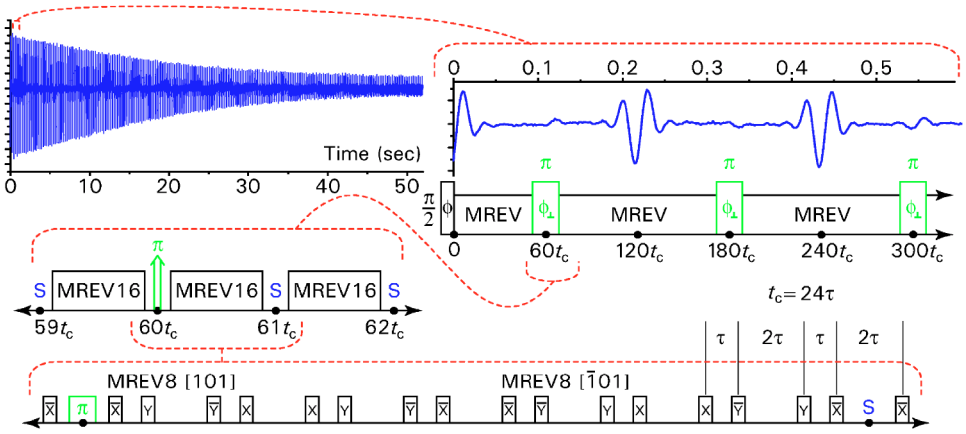

FIG. 1. (Color online) Schematic of the CPMG-MREV-16×120 pulse sequence with spin-echo data. The echoes shown in the upper left and expanded in the upper right are data from an isotopically natural single crystal of silicon. These are obtained by first exciting the sample with a $\pi/2$ pulse of arbitrary phase ϕ, decoupling with the MREV-16 sequence shown in detail on the bottom line, and refocusing with π pulses of phase $\phi_\perp=\phi+\pi/2$ every 120 cycles of MREV-16. The magnetization is sampled once per MREV-16 cycle in the windows marked with an S.

if a $\pi/2$ pulse about the x axis occurs in the pulse sequence, then simultaneously the toggling reference frame rotates by $\pi/2$ about the x axis. Correspondingly, an isolated nucleus periodically rotated by the MPS would be seen as stationary in the toggling reference frame. The internal terms of the Hamiltonian $\mathcal{H}_0$ and $\mathcal{H}_D$ are time dependent in this frame, and are therefore written

$$\tilde{\mathcal{H}}_0(t) = U_{rf}^\dagger(t)\mathcal{H}_0 U_{rf}(t), \tag{7}$$

$$\tilde{\mathcal{H}}_D(t) = U_{rf}^\dagger(t)\mathcal{H}_D U_{rf}(t), \tag{8}$$

where $U_{rf}(t)$ describes the unitary evolution due to the rf control sequence. Likewise, the coupling to the environment takes on an additional time dependence, leading to

$$\tilde{\mathcal{H}}_{env}(t) = -\hbar\gamma\sum_j \mathbf{b}(\mathbf{r}_j,t)\cdot U_{rf}^\dagger(t)\mathbf{I}_j(t)U_{rf}(t). \tag{9}$$

During some intervals of the multiple pulse sequence, the toggling frame and the rotating reference frame will be the same; it is during these intervals only that we measure the nuclear spin dynamics.

Flocquet's theorem tells us that the unitary time-evolution operator generated by the periodic, time-dependent internal Hamiltonian $\tilde{\mathcal{H}}_{int}(t)=\tilde{\mathcal{H}}_0(t)+\tilde{\mathcal{H}}_D(t)$ may be written $U_p(t)\exp(-iFt)$ where $U_p(t)$ is periodic with the same period. If we measure only once per period t_c ("stroboscopic observation"), then we are interested only in $U_p(mt_c)\times[\exp(-iFt_c)]^m$ for integers m. The prefactor $U_p(mt_c)$ is constant and may be neglected. In average Hamiltonian theory (AHT),[15] Ft_c is expanded in orders of t_c, the cycle time of the MPS, using the Magnus expansion:

$$Ft_c = \sum_{n=0}^{\infty}\bar{\mathcal{H}}^{(n)}t_c. \tag{10}$$

The nth-order average Hamiltonian may be written as time integrals of commutators of $\tilde{\mathcal{H}}_{int}(t)$; the zeroth-order term is simply the time average of $\tilde{\mathcal{H}}_{int}(t)$.

The sequence we employ in this study, illustrated at the bottom of Fig. 1, consists of 16 properly phased and separated $\pi/2$ pulses, forming MREV-16, a variant of the MREV-8 sequence.[16] With perfect pulses, the MREV-8 sequence results in the zeroth-order average internal Hamiltonian $\bar{\mathcal{H}}_{int}^{(0)}=-(1/3)\Sigma_j\hbar\omega_j(I_j^z\pm I_j^x)$, where the sign of the x component of the effective field depends on the helicity of the sequence. The MREV-16 sequence, shown in Fig. 1, concatenates each helicity of MREV-8, leading to the effective field terms

$$\bar{\mathcal{H}}_0^{(0)} = -\frac{1}{3}\sum_j \omega_j I_j^z, \tag{11}$$

$$\bar{\mathcal{H}}_0^{(1)} = \frac{\tau}{3}\sum_j \omega_j^2(I_j^x - 2I_j^y), \tag{12}$$

$$\bar{\mathcal{H}}_0^{(2)} = -\frac{\tau^2}{144}\sum_j \omega_j^3\left(3I_j^y - \frac{381}{2}I_j^z\right). \tag{13}$$

Here, $\tau=t_c/24$ as illustrated in Fig. 1. Although MREV-16 has reduced spectroscopic resolution over MREV-8 due to the smaller effective size of $\bar{\mathcal{H}}_0^{(0)}$, maintaining the effective field in the z direction (in zeroth order) allows easier nuclear control, and we are not interested in spectroscopy in the present study. The dipolar terms vanish in zeroth order; higher-order dipolar terms will be discussed in Sec. IV A.

We also tried a variety of other pulse sequences for decoupling, including BR-24,[17] CORY-48,[18] and SME-16.[19] Although we observed decoupling with all of these sequences,

MREV-16 showed the best performance, as we further discuss in Sec. IV.

The inhomogeneous offsets described by the dominant $\bar{\mathcal{H}}_0^{(0)}$ term cause static dephasing, which we periodically refocus by applying π pulses every 120 cycles of MREV-16. We employ the Carr-Purcell-Meiboom-Gill (CPMG) phase convention to correct for π-pulse errors,[20] as shown in Fig. 1. Such inserted pulses[21] would likewise be employed in an NMR quantum computer for decoupling and recoupling of multiple dipolar-coupled qubits.[11,22] We refer to this combined sequence as CPMG-MREV-16$\times$120.

2. Magic angle spinning

MAS decoupling operates on a slightly different mechanism from MPS. Rather than using rf to induce nuclear rotations, the sample is physically rotated about an axis at angle θ_{m} from the z axis. In the sample's reference frame, the dipolar coupling constants D_{jk} become time dependent; the only component of $D_{jk}(t)$ constant in time is proportional to $3\cos^2\theta_{\mathrm{m}}-1$, which is eliminated by choosing θ_{m} to be the "magic angle" that eliminates this term. Other terms of $D_{jk}(t)$ oscillate at multiples of the sample spinning speed. Again, one may expand the Flocquet Hamiltonian F in powers of the spinning cycle period $2\pi\Omega^{-1}$ and find that the spinning dipole Hamiltonian $\tilde{\mathcal{H}}_{\mathrm{D}}(t)$ averages to zero in zeroth order but not in higher orders. In particular, the first-order correction is present.[15]

C. Experimental details

Although MPS and MAS experiments are now routine in solid-state NMR, the application of these techniques to silicon introduces new challenges related to the low ^{29}Si NMR signal-to-noise ratio (SNR). The low signal results from a small gyromagnetic ratio γ, a sparse isotopic abundance (4.7% ^{29}Si in isotopically natural silicon), and, most importantly, an extremely long T_1. Silicon's long equilibration time makes averaging over multiple acquisitions impractical. Each echo time series in the present study was taken in a single measurement after thermal equilibration for one-half to five times T_1, except where noted. We compensated for the low SNR in these single-shot experiments by using large samples, which resulted in substantial inhomogeneous broadening and required large rf coils. The MPS experiments, however, required short rf pulses, which can be challenging when using large coils at high field.

1. MPS experiments

a. Apparatus. The MPS experiments were performed using an 89-mm-bore 7 T superconducting solenoid NMR magnet (Oxford) and a commercial NMR spectrometer (Tecmag) operating at 59.575 MHz. All experiments were performed at room temperature. We designed and built the probe to be as rigid and robust as possible for high-power rf, employing variable vacuum capacitors (Jennings) and high-power ceramic capacitors (HEC) embedded in plastic to accommodate average rf powers of approximately 800 W. The capacitors were placed as close to the coil as possible in a design that minimized arcing by shortening high-voltage leads. Using large capacitors near the coil allowed high SNR and flexible tuning for frequency and impedance matching. A small open BNC connector provided an antenna for direct monitoring of the rf field, which allowed us to symmetrize phase transients without NMR detection. We found that our results did not noticeably vary with asymmetric versus symmetric phase transients. Coil heating was a large concern, as the plastic coil holder would melt after about a minute of a high-power MPS; however, the probe tuning remained roughly constant as checked by continuous monitoring of the rf power reflected from the probe.

b. Spin locking. In these experiments, it is crucial to separate coherent oscillation from spin locking. Two kinds of spin locking are present in this experiment. Due to the finite pulse width and higher-order average Hamiltonian terms [see Eqs. (12) and (13)], the effective magnetic field witnessed by the nuclei is not exactly parallel to the z axis. Consequently, a magnetization spin locked to this effective field would have a small component in the xy plane which would be detectable under stroboscopic observation. This component was observed to decay very slowly, indicating a $T_{1\rho}$ of many minutes. To separate the coherent oscillations of the transverse field from this spin-locked signal, the rf was detuned about 120 Hz from the center of the nuclear resonance frequency. The transverse field was then seen to oscillate with a center frequency of $\Delta\omega\approx 40$ Hz, as expected from the zeroth-order average Hamiltonian. The small spin-locked "pedestal" shows no such oscillation, and was observed to change phase only when π pulses were applied. By Fourier transforming each echo, we were able to isolate the coherent oscillations, which appear as a broad peak at $\Delta\omega$ in each spectrum, from the spin-locked component, which appears as a spike at the center frequency. Decay curves were generated by integrating the detuned side peaks between half maxima. This procedure also eliminated the influence of pulse ringdown effects.

Pulsed spin locking[23] is a related effect which may be observed in samples undergoing rapid π pulses. This effect was observed when π pulses were applied every 5–10 cycles of MREV-16 and in spin-echo experiments without decoupling. The spin-locked decay time in this case was immeasurably long when π pulses were applied every 5 cycles, but rapidly decreased as the rate of π pulses was reduced. This effect can be deduced by careful observation of the phase of the signal after many π pulses; when pulsed spin locking is present, the phase of the signal near the tail of the decay is uncorrelated to the initial phase of the spins, as determined by the preparation pulse. We found pulsed spin locking to be present both when we used constant phase π pulses, as in the CPMG sequence, and when we used π pulses of alternating phase. For π pulses applied every 120 cycles, the effects of pulsed spin locking seem to be absent, although a very small tail in the echo decay is still present, presumably due to this effect.

c. Samples and coils. We used a variety of samples with different rf coils designed to maximize filling factor and rf homogeneity. We used an isotopically enhanced (96.9% ^{29}Si) cylindrical sample of single-crystal silicon; this sample and its NMR properties have been previously discussed.[24] We

also used a stack of polycrystalline silicon cylinders purchased from Alfa Aesar; these samples are free of impurities at the level of 0.1 ppm, with natural isotopic abundance (4.7% ^{29}Si). This stack was 2 cm long and 0.95 cm wide. We also investigated a smaller sample of isotopically depleted silicon, with between 0.98% and 1.3% ^{29}Si, varying across the sample. This sample, grown using the techniques described in Ref. 25, was a cylinder 6 mm in diameter and 2 cm long. It also featured 10^{17} cm^{-3} aluminum impurities introduced to shorten T_1 to allow signal averaging. With these samples, we used a 6-cm-long, 1-cm-diameter coil wound using 2-mm-diameter bare copper wire with variable pitch to improve rf homogeneity.[26] The coil was held firmly by a plastic coil form. The rf homogeneity was important for the longer samples; we characterized the homogeneity by measuring ^{29}Si Rabi oscillations using a similarly sized sample of solidified grease containing dimethyl siloxane. We found the free induction decay (FID) intensity for the antinode at pulse angle 450° to be 92% as strong as that at 90°, indicating moderate rf homogeneity. The $\pi/2$-pulse duration was 9 μs for this coil.

Our cleanest sample was a high-quality single crystal of silicon purchased from Marketech, also with natural isotopic abundance. This sample featured less than 5×10^{13} cm^{-3} *n*-type impurities. It was cut into a sphere of diameter 1.5 cm and fitted tightly in a constant-pitch coil approximately 6 cm long. The rf homogeneity for this coil over a spherical sample was roughly the same as the variable pitch coil over the cylindrical sample. The $\pi/2$-pulse duration was 15 μs for this coil.

We also investigated heavily doped wafers of metallic *n*-type silicon. These samples were convenient because the T_1 was only 50 s, unlike the purer samples for which we measured a T_1 of 4.5 h, consistent with earlier studies.[27] However, the SNR for the metallic silicon was always substantially lower, and decoupling sequences always performed poorly, even for powdered samples. We speculate that this is due to skin-depth effects.

2. MAS experiments

Power requirements were not an issue for MAS experiments, allowing the use of standard commercial equipment. These experiments were carried out using a commercial probe and spectrometer (Chemagnetics), in a 7 T magnet at room temperature. The magic angle was adjusted by measuring the locations of the methyl carbon and aromatic carbon peaks in the ^{13}C hexamethylbenzene MAS spectrum. By assuring that these peaks are within 0.2 ppm of their standard locations, the deviation from the magic angle is expected to be less than half a degree. Spinning rates were adjusted up to $\Omega/2\pi=5$ kHz; at rates higher than about 3.5 kHz the spinning became unstable. The CPMG refocusing sequence was employed to refocus inhomogeneous broadening, with varying pulse time. The $\pi/2$-pulse duration was 9 μs.

We studied an isotopically natural single-crystal silicon sample from the same growth as the spherical sample employed for the MPS experiments. The sample was cut into a cylinder 6 mm in diameter by 7 mm in height. Each MAS experiment was measured as a single shot after a 12 h thermalization time.

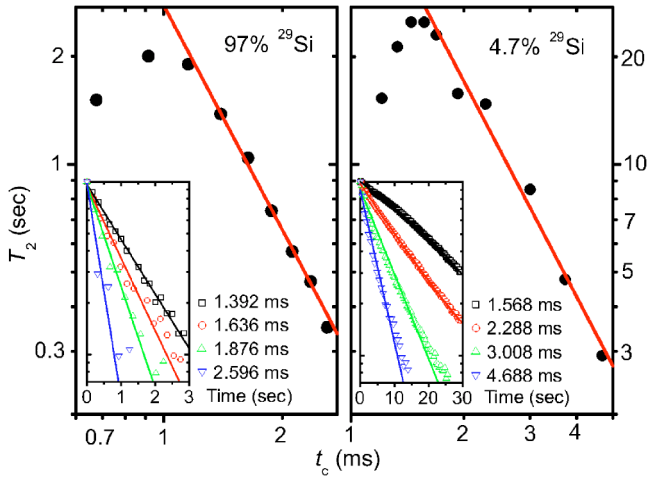

FIG. 2. (Color online) Coherence time versus cycle time in single-crystal silicon. The solid line is a fit showing the exponent -2.09 ± 0.07 for the isotopically enhanced sample (left) and -2.00 ± 0.2 for the isotopically natural sample (right). The insets show the integrated logarithmic magnitude of the spin echoes decaying in time for a few cycle times.

III. RESULTS

A. MPS experiments

As shown in Fig. 1, the CPMG-MREV-16$\times$120 sequence allows the observation of hundreds of spin echoes. Figure 2 shows the result of decoupling the single-crystal samples. The insets show the magnitude decay of the detuned echo; the data for both samples fit reasonably well to an exponential decay, as shown, and the resulting least-squares fit for each t_c is plotted. For the isotopically enhanced sample, the T_2 before decoupling is 450 μs for the [001] orientation, as reported previously for this sample.[24] The CPMG-MREV-16$\times$120 sequence extends the T_2 in this sample to nearly 2 s. For long t_c, the coherence time reduces as t_c^{-2}, indicating that decoherence is dominated by second-order terms in the average Hamiltonian; we discuss this result further in Sec. IV A. For short t_c, finite pulse width effects become more important, and the sequence fails.[14] In isotopically natural silicon single crystals, the coherence time is even longer due to the scarcity of ^{29}Si in the lattice. As shown in Figs. 1 and 2, the spin echoes in the sample last for as long as a minute, showing a T_2 of 25.0 ± 0.2 s. The effective Q of this qubit, then, is $\omega_0 T_2=10^9$, exceeding the Q of any other solid-state qubit, such as those based on Josephson junctions,[28–30] by at least four orders of magnitude.

Without decoupling, the T_2 of isotopically natural silicon as measured using only the CPMG sequence appears to be approximately 11 ms, although we do observe a long tail in the echo decay lasting several hundred milliseconds, as recently reported in other work.[9] The cause for this long tail is not well understood. However, we do not observe any fea-

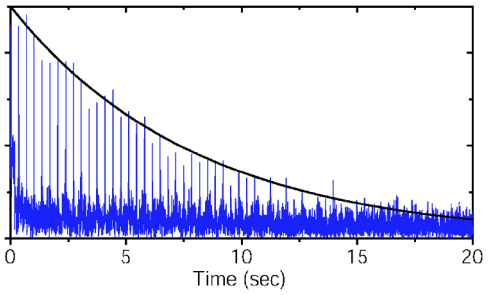

FIG. 3. (Color online) Spin echoes for isotopically depleted silicon. The solid line shows $\exp[-t/8\ \mathrm{s}]$, for comparison.

tures on this time scale when we apply decoupling, suggesting that this effect results only from the complexities of random dipolar couplings in the presence of inhomogeneous broadening and imperfect π pulses. We suspect that pulse errors are very significant, especially in heavily doped samples where skin-depth effects play an important role. The effects of pulsed spin locking, as discussed in Sec. II C, should not be discounted.

As the strength of the dipolar coupling is further decreased by isotopic depletion, the dipolar coupling constants D_{jk} become much smaller than the frequency offsets ω_j. The dominant second-order dipolar average Hamiltonian term leading to decoherence is then the dipolar/offset cross term, which scales as $\bar{\mathcal{H}}^{(2)} \propto t_c^2 |D_{jk}||\omega_j^2|$. For isotopic percentage p less than about 10%, we would expect T_2^{-1} to be proportional to the dipolar coupling constants, which vary as the inverse cube of the distance between ^{29}Si isotopes. Correspondingly, we expect $T_2^{-1} \propto p$, approaching T_1^{-1} as $p \to 0$. However, our attempt to observe this isotope effect was not successful. In the isotopically enhanced sample, the same decoupling sequence which led to $T_2 = 25$ s in isotopically natural silicon led to a decay time not exceeding 8 s, as shown in Fig. 3. These noisy data result from ten averages in one experiment lasting a week. We believe the reduced T_2 is due to the presence of lattice defects in the sample.

Similar data are observed in the sample of pure, polycrystalline silicon. Although the shallow impurity content of this sample is very low, leading to $T_1 = 4.5$ h, the CPMG-MREV-16$\times$120 sequence leads to a decoherence time scale of approximately 8 s. The higher SNR for this isotopically natural sample allowed us to study this decay more carefully. There are two unusual features of these data, both revealed in Fig. 4. First, the decay curve is neither exponential nor Gaussian. Second, this decay curve retains its shape as t_c is altered. If this decay were due to residual dipolar coupling terms of the average Hamiltonian, some change in shape would be expected. We conclude that this decoherence is due to low-frequency noise intrinsic to the sample. In Sec. IV B we argue that the same thermal processes at defects which lead to $1/f$ charge noise are responsible for these unusual data. Our data in isotopically depleted silicon could be due to the same type of decoherence.

B. MAS experiments

The T_2 times in single-crystal silicon observed under MAS were not as long as in the MPS experiments. The observed decay is exponential with $T_2 = 2.6$ s at the fastest spinning speeds. We observe this decay to be independent of the π-pulse timing, as expected for dipolar couplings. The T_2 as a function of rotating speed Ω is shown in Fig. 5. The T_2 varies roughly linearly with Ω, as expected from first-order AHT and consistent with typical MAS results.[31]

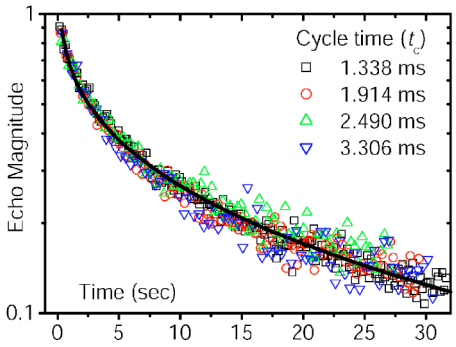

FIG. 4. (Color online) Echo decay curves for pure polycrystalline silicon of natural isotopic abundance. No significant variation in the data is observed as t_c is changed. The solid line is a fit to the function described in Sec. IV B.

IV. DISCUSSION

We now discuss the physical mechanisms for the observed residual T_2 after decoupling. In Sec. IV A, we discuss the source of decoherence observed in *single-crystal* silicon. In both MPS and MAS experiments, and for both isotopically enhanced and isotopically natural single crystals, this decoherence source is residual dipolar couplings. In Sec. IV B, we present the model for the decoherence source in *polycrystalline* silicon.

A. Residual dipolar decoherence

Both MREV-16 and MAS have first-order dipolar corrections in AHT. However, in the MREV-16 experiment in single-crystal silicon, we observe only second-order effects.

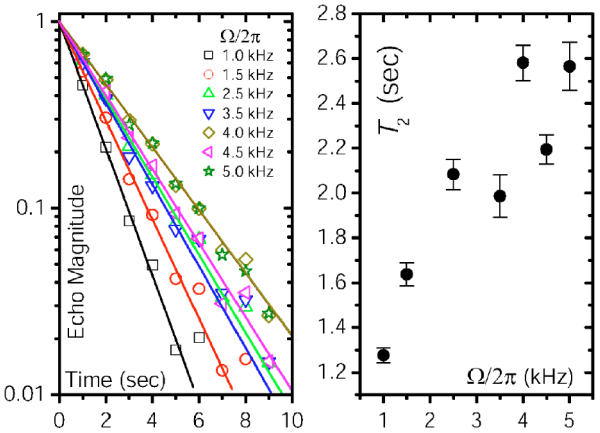

FIG. 5. (Color online). The decay of the spin-echo peaks under MAS for several rotation speeds Ω, with exponential fits (left), and the observed decay times T_2 plotted against Ω (right).

Since the offset term of the Hamiltonian is substantially larger than the dipole term, we believe this is due to the effects of second averaging,[32] as we now explain.

The first-order average Hamiltonian under MREV-16 may be written

$$\overline{\mathcal{H}}_{\mathrm{D0}}^{(1)} = \frac{-i}{2t_c}\int_0^{t_c} dt_2 \int_0^{t_2} dt_1 [\tilde{\mathcal{H}}_{\mathrm{int}}(t_1), \tilde{\mathcal{H}}_{\mathrm{int}}(t_2)] = \frac{1+2i}{3}\tau\left[\frac{1}{2}\sum_j \omega_j^2 I_j^+ + \sum_{j\neq k} D_{jk}(\omega_j - \omega_k) I_j^+ I_k^z\right] + \mathrm{H.c.} \tag{14}$$

The first term represents a transverse effective field; we have already seen this term as Eq. (12). The second term, the dipolar/offset term, would result in dipolar decoherence. However, since we apply our pulses off resonance, the dominant term in the Hamiltonian is the zero-order offset term of Eq. (11). In a reference frame omitting the dynamics of this most important term (a frame coincident with observation of spin echoes), every term in Eq. (14) becomes time dependent and may be considered to average to zero. The lowest-order *secular* terms appear in second order, consistent with our data.

The importance of this second averaging may explain why more sophisticated pulse sequences such as BR-24 and CORY-48 failed to outperform MREV-16. We find that the first-order dipolar-offset cross term in BR-24 and CORY-48 both have secular terms in the presence of heavy inhomonegeous broadening.

A remaining question is why the MPS experiments outperformed the MAS experiments. A rough comparison, following AHT, may be made as follows. For heavily inhomogeneously broadened samples, the leading order average Hamiltonian leading to decoherence under MAS is the first-order dipolar/offset cross term, $\overline{\mathcal{H}}_{\mathrm{D0}}^{(1)}$, which is of order $\sim t_c T_2^{-1}(T_2^*)^{-1}$. Here, T_2 is the undecoupled decoherence rate and T_2^* is the FID decay time due to inhomogeneous dephasing. Under CPMG-MREV-16×120, the leading order term after second averaging, as discussed above, is $\overline{\mathcal{H}}_{\mathrm{D00}}^{(2)} \sim t_c^2 T_2^{-1}(T_2^*)^{-2}$. If the cycle time for the MPS is comparable to the rotation period for MAS, and if the field inhomogeneity is approximately the same for both experiments, then MPS may be expected to outperform MAS if its cycle time is substantially faster than T_2^*. This condition seems to be met in our experiments. A more careful experimental comparison, however, would have to be performed in the same apparatus, so that inhomogeneities are the same in both experiments.

B. Decoherence due to $1/f$ noise

The observation of T_2 due to residual dipolar terms, as discussed in the previous section for single-crystal silicon, is typical of NMR. A more atypical result of the present study is the nonexponential, t_c-independent decoherence in pure polycrystalline silicon samples. We believe this decoherence is due to the same low-frequency noise source that leads to $1/f$ noise in silicon wafers.[33] This noise is attributed to charge traps at lattice defects and other deep impurities, which lead to fluctuations of the diamagnetic shielding seen at nearby nuclei.

To discuss the t_c dependence, we use the cumulant expansion approach[34] to derive a formula for T_2 due to a classical fluctuating local field $\mathbf{b}(\mathbf{r}_j,t)$ in the presence of a MPS. The periodic, rf-induced evolution of the interaction Hamiltonian in the toggling frame, Eq. (9), is described by a Fourier expansion. The local random magnetic field at the jth nucleus, $\mathbf{b}(\mathbf{r}_j,t)$, is assumed to fluctuate according to a Markov process with correlation time Γ_j, so that

$$\gamma^2 \langle b^z(\mathbf{r}_j,\tau) b^z(\mathbf{r}_j,0)\rangle = \Delta_j^2 e^{-\Gamma_j \tau}, \tag{15}$$

where Δ_j^2 is the variance of the frequency shift due to this fluctuating field. The details of this calculation are in Appendix B; the result is

$$\frac{1}{T_{2j}} = \frac{\Delta_j^2}{2}\sum_{n=-\infty}^{\infty} A_n^{zz} \frac{\Gamma_j}{\Gamma_j^2 + (2\pi n i/t_c)^2}, \tag{16}$$

where the Fourier coefficient A_n^{zz} is found by

$$A_n^{zz} = \frac{1}{t_c}\int_0^{t_c} \frac{\mathrm{Tr}\{U_{\mathrm{rf}}^\dagger(t) I_j^z U_{\mathrm{rf}}(t) I_j^z\}}{I(I+1)/3} e^{-2\pi i n t/t_c} dt. \tag{17}$$

Equation (16) indicates to us that if most spins see a correlation time Γ_j that is smaller than or of the same order as t_c^{-1}, then the observed T_2 should depend on t_c, in contrast to our data for polycrystalline silicon shown in Fig. 4. Our data would seem to be explained by processes with Γ_j much larger than t_c^{-1}, in which case $T_{2j} \propto \Gamma_j$.

The assumption $\Gamma_j \gg t_c^{-1}$ is the common "motional narrowing" or "white-noise" limit for this T_2 noise process. However, the noise is not strictly white at frequencies higher than t_c^{-1}; in particular, it is unlikely to have a significant component near the Larmor frequency ω_0, since T_1, as given by the same approach in Eq. (B7), will then yield a value similar to T_{2j}, unless $\mathbf{b}(\mathbf{r}_j,t)$ is highly anisotropic. Correspondingly, free carriers and fixed dipolar paramagnetic impurities are unlikely to be responsible for the observed intrinsic T_2, since these are well known to lead to isotropic magnetic noise with correlation times much shorter than the Larmor period. These sources are undoubtedly present and are likely the cause of the observed T_1.[35]

The physical picture we suggest for T_2 decoherence is as follows. Defect states are thermally charged and discharged. The resulting unpaired spins in such states rapidly fluctuate with correlation times far faster than ω_0, explaining the observed field independence of T_1 but having little effect on T_2, since the spin fluctuations are too fast. Rather, the much slower charging and discharging of these defect states changes the diamagnetic shielding at nearby nuclear sites, causing "chemical shifts" of order <1 ppm. This fluctuating chemical shift is the cause of decoherence via spectral diffusion. The cumulant expansion approach leading to Eq. (16) is not appropriate for fluctuations that are very slow in comparison to the measurement time; however, the t_c independence of the data suggests that the dominant source of this decoherence is processes much faster than t_c. These faster processes *are* well described by the cumulant expansion ap-

proach, and since $\Sigma_n A_n^{zz}=1$, we presume they lead to a local decoherence rate given by

$$\frac{1}{T_{2j}} \approx \frac{\Delta_j^2}{2\Gamma_j}. \tag{18}$$

Although Eq. (18) is sufficient for our purposes, we also clarify the issue of time scales with another, nonperturbative approach[36] which neglects the fast MREV-16 pulse sequence but accounts for the slower refocusing effects of the π pulses. In this approach, the decay function with a single refocusing π pulse (Hahn echo) at the $2\tau_e$ echo peak and with frequency shifts fluctuating according to a Poisson random pulse train is given by

$$\langle e^{i\phi(2\tau_e)}\rangle = e^{-2\tau_e\Gamma_j}\left[\frac{\cosh(2\tau_e\Gamma_j\sqrt{1-g_j^2})-g_j^2}{1-g_j^2} + \frac{\sinh(2\tau_e\Gamma_j\sqrt{1-g_j^2})}{\sqrt{1-g_j^2}}\right], \tag{19}$$

where $g_j=\Delta_j/\Gamma_j$. This result assumes a single π pulse; if we examine the more complicated equations for a train of π pulses, we find results comparable to assuming that unrefocused coherence is forgotten every echo cycle,[37] so that

$$\langle e^{i\phi(2n\tau_e)}\rangle \approx \langle e^{i\phi(2\tau_e)}\rangle^n. \tag{20}$$

Although time is measured discretely at the peak of each echo, we will set $t=2n\tau_e$ and treat it as continuous. However, the value of $\tau_e=120t_c$ in comparison to other time scales is critical, as evidenced by the following argument. Suppose nucleus k is coupled to a fluctuator that is slow in comparison to the chemical shift, so that $\Gamma_k \ll \Delta_k$. In this $g_k \to \infty$ limit, Eqs. (19) and (20) give

$$\langle e^{i\phi_k(t)}\rangle \to \exp\left(-\frac{4\Delta_k^2\tau_e^2\Gamma_k}{3}t\right). \tag{21}$$

Now suppose nucleus j is coupled to a very fast fluctuator, with $\Gamma_j \gg \Delta_j$. In this $g_j \to 0$ limit we find

$$\langle e^{i\phi_j(t)}\rangle \to \exp\left(-\frac{\Delta_j^2}{2\Gamma_j}t\right), \tag{22}$$

the same result as Eq. (18) derived using the toggling frame cumulant expansion in the $\Gamma_j \gg t_c^{-1}$ limit. We now ask whether nucleus j or k contributes more heavily to the observed ensemble signal. In our model, nuclei dephase independently, and the *sum* of their decay functions provides the signal. Consequently, those spins that decay the *slowest* contribute to the signal the most.[38] Thus we compare decay rates for our two spins:

$$\frac{T_{2j}}{T_{2k}} = \frac{8}{3}\frac{\Delta_k^2}{\Delta_j^2}\Gamma_j\Gamma_k\tau_e^2. \tag{23}$$

If τ_e is larger than the geometric average of the two fluctuator rates, we find that the nuclei coupled to fast oscillators will dominate the sum, as these decay the slowest. The data's independence of $\tau_e=120t_c$ indicates that we are working in this regime, i.e., that our signal is dominated by spins close to fast oscillators causing rapid spectral diffusion. This is the limit where the perturbative cumulant expansion approach agrees with the nonperturbative approach of Eq. (19). In the following, then, we assume that our signal is dominated by nuclei decaying according to Eq. (18).

We now introduce a distribution of Γ_j across the sample by assuming that the charging/discharging processes leading to this nuclear decoherence are the same as those which are well known to lead to $1/f$ noise near silicon surfaces. The standard model for $1/f$ noise supposes that across the sample, Γ_j is randomly distributed according to the probability density function

$$D_\Gamma(\gamma) = \begin{cases} [\gamma \ln(\Gamma_{high}/\Gamma_{low})]^{-1}, & \Gamma_{low} < \gamma < \Gamma_{high}, \\ 0 & \text{otherwise}. \end{cases} \tag{24}$$

It may be easily seen that this distribution leads to $1/f$ charge noise for $\Gamma_{low} \ll f \ll \Gamma_{high}$. The details of the physical processes leading to this distribution in silicon are discussed in Ref. 33

We presume our nuclei are dephased by a random selection of bistable oscillators with lifetime Γ_j. We also presume the nuclei undergo random shifts Δ_j, and since isotope placement is diffuse and random, we assume Δ_j will be mostly uncorrelated with Γ_j (corresponding to roughly one impurity per nucleus). We therefore arrive at the ensemble decay function

$$\sum_j \langle e^{i\phi_j(t)}\rangle \approx \int d\delta D_\Delta(\delta)\int d\gamma D_\Gamma(\gamma)\exp\left(-\frac{\delta^2}{2\gamma}t\right) = \int d\delta D_\Delta(\delta)\frac{E_1(\delta^2 t/2\Gamma_{high}) - E_1(\delta^2 t/2\Gamma_{low})}{\ln(\Gamma_{high}/\Gamma_{low})}, \tag{25}$$

where $E_1(x)$ is the exponential integral $\int_x^\infty dx\, e^{-x}/x$. The $E_1(\delta^2 t/2\Gamma_{low})$ term is much smaller than the $E_1(\delta^2 t/2\Gamma_{high})$ if $\Gamma_{high} \gg \Gamma_{low}$, as appears to be the case for $1/f$ noise observed in silicon, so we neglect this term. For the distribution of frequency shifts $D_\Delta(\delta)$, we assume that δ is peaked around some average $\langle\Delta\rangle$. We thus expand the integrand about this average to lowest order, allowing us to complete the δ integral without detailed knowledge of the distribution:

$$\sum_j \langle e^{i\phi_j(t)}\rangle \approx N^{-1}[E_1(\alpha t) + \beta(1+2\alpha t)\exp(-\alpha t)], \tag{26}$$

where $\alpha=\langle\Delta\rangle^2/2\Gamma_{high}$ and $\beta=\langle\Delta\rangle^2/\langle\Delta\rangle^2-1$. (The normalization constant N would be a free parameter for any model, since the magnitude of our data shifts from experiment to experiment due to differing initial magnetizations and probe temperatures.) This function has the correct shape for our data; we also reproduce its shape with computer simulations of the decoherence model described.

Figure 4 shows this theoretical curve, fitted to the data by the Levenberg-Marquadt method for least-squares fitting. We find insignificant difference between fitting all four experimental curves separately or fitting all the data simultaneously. The curve shown fits all the data assuming shared

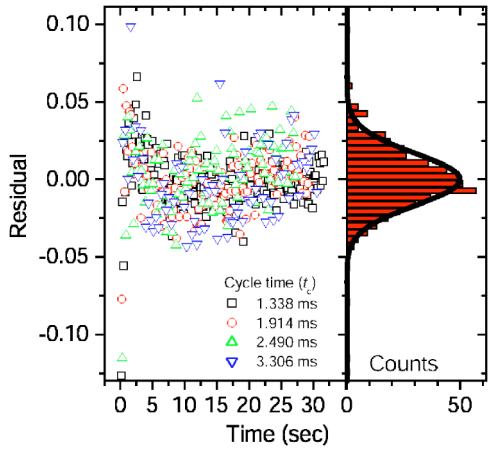

FIG. 6. (Color online). Residuals versus time. The deviation of the data from the fitting function of Eq. (26), with a histogram of those residuals on the right, consistent with Gaussian noise.

constants α, β but independent normalization constants N for a total of six fitting parameters over 493 data points. The residuals are shown in Fig. 6, where they are checked against Gaussian noise with a χ^2 test.[39] The first two echoes are slightly weaker than the theoretical curve, and systematically deviate from the model. This is not surprising, since we omitted the effects of those spins which decay more rapidly due to slower spectral diffusion in the derivation of Eq. (26). Otherwise, we find that the residuals are consistent with $\sigma=0.02$ Gaussian noise with a χ^2 of 1.09 over 16 bins, leaving no indication of systematic disagreement between the data and the model.

The parameter fit is optimized at $\alpha=22\pm2$ mHz and $\beta=0.20\pm0.05$. This value of α would be consistent, for example, with an average chemical shift of $\sim$0.5 ppm and a cutoff rate constant $\Gamma_{\text{high}}\sim300$ kHz. In the Dutta-Horn model for $1/f$ noise,[40] we would expect $\Gamma_{\text{high}}\propto\exp(-E/kT)$, where E is an energy barrier for the fastest charge traps in the sample. This model thus predicts an exponential temperature dependence for this decoherence rate.

In summary, we find that our data in polycrystalline silicon is consistent with our model for decoherence induced by $1/f$ charging processes superimposed over unbiased Gaussian noise. This decoherence source should diminish in single crystals, as shown in our single-crystal data, and at low temperatures.

V. CONCLUSION

Our results have relevance for potential silicon-based quantum computers for two reasons. First, our CPMG-MREV-16$\times$120 experiment showed that, even at room temperature, nuclear coherence times exceed at least 25 s in single crystals, a modest lower bound for what is possible after isotopic depletion, sample cooling, and pulse sequence optimization. Second, the same experiment in polycrystalline silicon revealed experimentally the decoherence source that is likely to dominate silicon-based NMR computers: magnetic fluctuations due to $1/f$ noise at silicon surfaces. We believe this result provides a first step in characterizing this decoherence in order that it may be avoided in potential devices. The elimination of $1/f$ noise from oxides and interfaces poses a critical fabrication challenge in quantum computing designs based on semiconductor impurities[8,41] and Josephson junctions,[28–30] but this noise is expected to be very small in high-quality bulk single-crystal silicon at low temperature.

Decoupling pulse sequences such as those used here have been proposed for nuclear memory in high-mobility GaAs/AlGaAs heterostructures.[42] We caution that the large rf power required to effectively decouple the ubiquitous nuclear spins in this system may be inconsistent with millikelvin operation, even if small, high-Q coils and low-power, windowless sequences[43] are employed. For this reason, we believe isotopically depleted silicon to be a more promising material for nuclear quantum memory, assuming that efficient methods for transferring quantum information to and from its well-isolated nuclei can be found. The results presented here indicate no serious obstacle for the use of silicon nuclei as robust quantum memory in future devices.

ACKNOWLEDGMENTS

The work at Stanford was sponsored by the DARPA-QuIST program. T.D.L. was supported by the Fannie and John Hertz Foundation. The work at Keio was partially supported by the Grant-in-Aid for Scientific Research in Priority Areas, Semiconductor Nanospintronics, No. 14076215. E.A. and K.M.I. thank the technical staff of the Central Research Facility of Keio University for the assistance with the MAS NMR measurements. We also thank N. Khaneja, R. de Sousa, C. Ramanathan, and D. G. Cory for useful discussions.

APPENDIX A: ENSEMBLE VS SINGLE-SPIN MEASUREMENT

We have compared our results for measurement of the T_2 decay of an ensemble of nuclei to the results of decoherence measurements of single qubits, but there are differences between ensemble measurements and single-qubit measurements. Important differences could include the practicality of each measurement method, the effect of back action, and the sensitivity to initial conditions. Even if measurement artifacts due to such factors are neglected, though, a fundamental difference between the two measurement types remains. We discuss this difference using the following formalism.

By definition, single-qubit decoherence is the uncontrolled decay of off-diagonal elements of the qubit density matrix in the logical basis. To be precise, let us denote by $\rho_j(t)$ the density matrix of the system after tracing over all degrees of freedom other than the jth qubit. The off-diagonal components are given by the function

$$G_j(t)=\frac{\mathrm{Tr}\{I_j^+\rho_j(t)\}}{\mathrm{Tr}\{I_j^+\rho_j(0)\}}. \tag{A1}$$

The magnitude of this function will decay in the presence of decoherence. If single-nuclear-spin measurement were pos-

sible, then $|G_j(t)|$ is the decay function that we would construct by initializing a single spin in the same state many times, measuring its x and y spin projections (in separate experiments) at different times t, and averaging the results of an ensemble of experiments.

When we make a heterodyne NMR measurement of N spins evolving according to some pulse sequence, our observable is $\Sigma_{j=1}^{N} I_j^+$. In this discussion, we neglect the small variation in measurement strengths for each spin due to rf inhomogeneity. When we examine the magnitude $|M(t)|$ of the measured magnetization, we obtain

$$|M(t)|^2 = \frac{\sum_{j=1}^{N} G_j(t) \sum_{k=1}^{N} G_k^*(t)}{\sum_{j=1}^{N} G_j(0) \sum_{k=1}^{N} G_k^*(0)}. \tag{A2}$$

If we assume that each qubit begins in the same initial state, as occurs in our sequence, this may be simplified to

$$|M(t)|^2 = \frac{1}{N^2} \sum_j |G_j(t)|^2 + \frac{1}{N^2} \sum_{j \neq k} G_j(t) G_k^*(t). \tag{A3}$$

The first term may be recognized as an average of single-spin measurement results. The second term may recognized as an interference term. As a simple example of this formalism, suppose there is only inhomogeneous broadening with no refocusing π pulses (so that each qubit oscillates at its own frequency ω_j) but otherwise no decoherence. Then $G_j(t) = \exp(i\omega_j t)$ and

$$|M(t)|^2 = \frac{1 + N^{-1} \sum_{j \neq k} e^{i(\omega_j - \omega_k)t}}{N} \rightarrow e^{-2t/T_2^*}. \tag{A4}$$

The presence of inhomogeneous broadening is the most obvious difference between an ensemble and a single-spin measurement; hence the π pulses used to refocus such effects are crucial. As noted in Sec. IV A, inhomogeneous broadening continues to play a limiting role for decoherence in second-order AHT.

The principal question now is whether the dynamics in our system cause *constructive* or *destructive* interference in the second term of Eq. (A3). We would expect constructive interference in a system of high symmetry such as dipolar coupling in CaF_2; here the ensemble average is equivalent to a series of single-spin measurements, and the oscillatory character of the dipolar dynamics is revealed in experiments.[44] However, in isotopically natural silicon, the nuclear-nuclear couplings are random. When dipole-dipole couplings are the source of decoherence, as in our experiments in single crystals, each spin undergoes different oscillations in its own dipolar environment, and destructive interference is seen. Therefore, the dipole-limited coherence times we observe are underestimates for what one might observe through a series of single-spin measurements on a typical nucleus, for which more oscillatory decay curves would be expected. To illustrate this argument, we show in Fig. 7 the result of a simulation of eight spins evolving according to a dipolar coupling with couplings drawn randomly from a uniform distribution between $-D_0/2$ and $D_0/2$. While the initial decay observed in $|M(t)|$ represents the average of the initial decay of the individual spin measurements $G_j(t)$, the sum $|M(t)|$ masks the longer-lived oscillations observable in individual spin measurements.

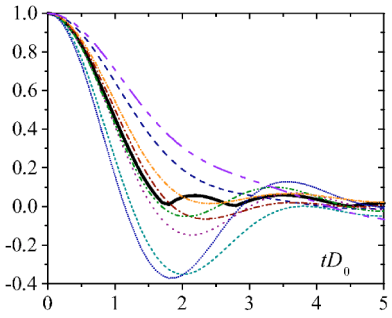

FIG. 7. (Color online) Simulated dipolar decoherence versus time. The broken lines represent individual spin measurements $\mathrm{Re}\{G_j(t)\}$ on an eight-spin simulation of dipolar evolution with uniformly random coupling constants with range $[-D_0/2, D_0/2]$. The solid line is the magnitude sum $|M(t)|$.

When spectral diffusion is the leading cause of decoherence, single-spin decoherence would also be recovered in the ensemble measurement if each qubit witnessed the same noise spectral density. A canonical example of such *homogeneous* broadening is Doppler broadening in the optical spectroscopy of gases. In contrast, our model for spectral diffusion in polycrystalline silicon, discussed in Sec. IV B, proposes that the random fluctuating environment seen by each nucleus is different, depending on both the lifetime of the electronic fluctuation near each nucleus and the frequency shift it causes. Hence a spin-echo experiment on a single spin might result in a decay from one echo to the next given by Eq. (19), whereas a sum over many such spins yields the different function of Eq. (26). In this case the more rapidly diffusing spins contribute less to the ensemble average, and therefore the observed coherence times represent overestimates for what one might observe through a series of single-spin measurements on a typical nucleus.

APPENDIX B: CUMULANT EXPANSION IN THE TOGGLING FRAME

Nuclear relaxation is often theoretically described by a cumulant expansion approach,[34] which we employ here to analyze the importance of the MPS on T_2 relaxation due to a classically fluctuating field. In this approach, we seek the time dependence of $I_j^+ = I_j^x + iI_j^y$ from an initial state in which the spin begins in the transverse plane, as this is the measured observable with heterodyne detection of a toggling-frame FID experiment. We thus seek a phase decay for the jth spin, which is formally defined by

$$\langle e^{i\phi_j(t)} \rangle = \frac{\langle \mathrm{Tr}\{U_{\mathrm{env}}^\dagger(t) I_j^+ U_{\mathrm{env}}(t) I_j^-\} \rangle}{\mathrm{Tr}\{I_j^+ I_j^-\}}, \tag{B1}$$

where $U_{\mathrm{env}} T \exp(-i\int_0^t \tilde{\mathcal{H}}_{\mathrm{env}}(t')dt'/\hbar)$. Here, $\langle \cdot \rangle$ refers to averaging over the classical random fields. To evaluate this function perturbatively, we assume

$$\langle e^{i\phi_j(t)}\rangle = \exp[\Psi_j(t)],$$

and expand $\Psi_j(t)$ in powers of the small perturbative Hamiltonian $\tilde{\mathcal{H}}_{\rm env}(t)$. The lowest-order result may be written[44]

$$\langle e^{i\phi_j(t)}\rangle \approx \exp\left(-\int_0^t (t-\tau)\frac{\langle \mathrm{Tr}\{[I_j^+,\tilde{\mathcal{H}}_{\rm env}(\tau)][\tilde{H}_{\rm env}(0),I_j^-]\}\rangle}{\hbar^2\,\mathrm{Tr}\{I_j^+I_j^-\}}d\tau\right). \tag{B2}$$

The environment-coupling Hamiltonian in the rotating, toggling reference frame, $\tilde{\mathcal{H}}_{\rm env}(t)$, contains two kinds of terms, which vary by the frequency at which the constitutent spin operators oscillate due to the rotating and toggling frame transformations. There are the longitudinal terms, proportional to I_j^z, and the transverse terms, proportional to $I_j^{\pm}(t)$. All components oscillate according to the periodic rotations incurred by the pulse sequence; for these oscillations, we imagine expanding each spin operator in a Fourier series. For example, I_j^z in the rotating, toggling frame is written

$$U_{\rm rf}^{\dagger}(t)I_j^zU_{\rm rf}(t) = \sum_{n=-\infty}^{\infty}\sum_{\alpha=x,y,z} A_n^{z\alpha}e^{2\pi nit/t_c}I_j^{\alpha}. \tag{B3}$$

The transverse spin components, however, also oscillate at $\omega/2\pi = 59.575$ MHz, the fastest frequency in the system. Thus the transverse components are written

$$U_{\rm rf}^{\dagger}(t)I_j^{\pm}(t)U_{\rm rf}(t) = e^{\pm i\omega t}\sum_{n=-\infty}^{\infty}\sum_{\alpha=x,y,z} A_n^{\pm\alpha}e^{2\pi nit/t_c}I_j^{\alpha}, \tag{B4}$$

where $A^{\pm\alpha}=A^{x\alpha}+iA^{y\alpha}$. Thus, Eq. (B2) may be expanded as

$$\langle e^{i\phi_j(t)}\rangle = \exp\left(-\frac{\gamma^2}{2}\sum_{n=-\infty}^{\infty}\sum_{s,r=0,\pm1}\frac{A_n^{sr}}{1+s^2}\int_0^t (t-\tau) \times\langle b^{-s}(\mathbf{r}_j,t)b^r(\mathbf{r}_j,0)\rangle e^{i(s\omega+2\pi ni/t_c)t}d\tau\right). \tag{B5}$$

We now assume that the components of $\mathbf{b}(\mathbf{r}_j,t)$ are uncorrelated, and assume cylindrical symmetry about the magnetic field, simplifying the sum over coordinates to

$$\langle e^{i\phi_j(t)}\rangle = \exp\left[-\frac{\gamma^2}{2}\sum_{n=-\infty}^{\infty}\left(A_n^{zz}\int_0^t (t-\tau) \times\langle b^z(\mathbf{r}_j,\tau)b^z(\mathbf{r}_j,0)\rangle e^{2\pi nit/t_c}d\tau + \sum_{s=\pm}\frac{A_n^{s,-s}}{2}\int_0^t (t-\tau) \times\langle b^{-s}(\mathbf{r}_j,\tau)b^s(\mathbf{r}_j,0)\rangle e^{i(s\omega_0+2\pi n/t_c)t}d\tau\right)\right]. \tag{B6}$$

A similar calculation for T_{1j}, the thermal relaxation time for the jth spin, yields

$$e^{-t/T_{1j}} = \exp\left(-\frac{\gamma^2}{2}\int_0^t (t-\tau)\sum_{s=\pm}\langle b^{-s}(\mathbf{r}_j,\tau)b^s(\mathbf{r}_j,0)\rangle e^{\pm i\omega_0\tau}d\tau\right). \tag{B7}$$

Although T_1 has been measured as 4.5 h for the sample in question, this bulk result is a consequence of both the relaxation of individual spins and spin diffusion. However, spin diffusion occurs on a time scale $T_2\sim 10$ ms$\ll T_1$. Therefore, the thermal relaxation of individual spins must be on the order of hours. The second term of Eq. (B6) may be recognized as a T_1 term (lifetime broadening), and may be neglected in the current discussion.

We now use the autocorrelation function for a Markov process, Eq. (15). The important result of the cumulant expansion is the limit $t\gg\Gamma_j^{-1}$, where the time is sampled much more slowly than the fluctuations in $b^z(\mathbf{r}_j,t)$. Then we find that each spin loses phase coherence with time scale T_{2j} as given by Eq. (16).

It is important to remember that this theory is not sufficient for describing very slow fluctuations, for two reasons. First, we assumed the fluctuation time scale is much slower than the measurement time. Second, very slow fluctuations are partially refocused by the π pulses, a process not accounted for in this approach.

*Electronic address: tladd@stanford.edu
†Currently at Max-Planck-Institut für Festkörperforschung, D-70569, Stuttgart, Germany.
‡Also at National Institute of Informatics, Tokyo, Japan.

[1] M. A. Nielsen and I. L. Chuang, *Quantum Computation and Quantum Information* (Cambridge University Press, Cambridge, U.K., 2000).
[2] P.W. Shor, Phys. Rev. A **52**, R2493 (1995); A. M. Steane, Phys. Rev. Lett. **77**, 793 (1996).
[3] P.W. Shor, in *Proceedings, 37th Annual Symposium on Fundamentals of Computer Science (FOCS)* (IEEE Press, Los Alamitos, CA, 1996), p. 56.
[4] D. P. DiVincenzo, Science **270**, 255 (1995).
[5] N. A. Gershenfeld and I. L. Chuang, Science **275**, 350 (1997); D. G. Cory, A. F. Fahmy, and T. F. Havel, Proc. Natl. Acad. Sci. U.S.A. **94**, 1634 (1997).
[6] B. Sapoval and D. Lepine, J. Phys. Chem. Solids **27**, 115 (1966).
[7] T. D. Ladd, J. R. Goldman, F. Yamaguchi, Y. Yamamoto, E. Abe, and K. M. Itoh, Phys. Rev. Lett. **89**, 017901 (2002).
[8] B. E. Kane, Nature (London) **393**, 133 (1998).
[9] A. E. Dementyev, D. Li, K. MacLean, and S. E. Barrett, Phys. Rev. B **68**, 153302 (2003); S. Watanabe and S. Sasaki, Jpn. J.

Appl. Phys., Part 2 **42**, L1350 (2003).
[10] K. M. Itoh *et al.*, Jpn. J. Appl. Phys., Part 1 **42**, 6248 (2003).
[11] F. Yamaguchi, T. D. Ladd, C. P. Master, Y. Yamamoto, and N. Khaneja, (unpublished).
[12] C. Ramanathan, H. Cho, P. Cappellaro, G. S. Boutis, and D. G. Cory, Chem. Phys. Lett. **369**, 311 (2003).
[13] A. Abragam, *Principles of Nuclear Magnetism* (Clarendon Press, Oxford, 1961).
[14] M. Mehring, *Principles of High Resolution NMR in Solids* (Springer-Verlag, Berlin, 1983).
[15] U. Haeberlen and J. S. Waugh, Phys. Rev. **175**, 453 (1968).
[16] P. Mansfield, M. J. Orchard, D. C. Stalker, and K. H. B. Richards, Phys. Rev. B **7**, 90 (1973); W.-K. Rhim, D. D. Elleman, and R. W. Vaughan, J. Chem. Phys. **59**, 3740 (1973).
[17] D. P. Burum and W. K. Rhim, J. Chem. Phys. **71**, 944 (1979).
[18] D. G. Cory, J. B. Miller, and A. N. Garroway, J. Magn. Reson. (1969-1992) **90**, 205 (1990).
[19] G. S. Boutis, P. Cappallaro, H. Cho, C. Ramanathan, and D. G. Cory, J. Magn. Reson. **161**, 132 (2003).
[20] S. Meiboom and D. Gill, Rev. Sci. Instrum. **29**, 6881 (1958).
[21] We note that the CPMG convention changes the sequence according to the initial phase of the nuclear qubit, which is incompatible with the memory of unknown or entangled quantum states. However, more complex NMR techniques such as composite pulses are known to allow phase-independent pulse correction [M. H. Levitt and R. Freeman, J. Magn. Reson. (1969-1992) **43**, 65 (1981)]. The MREV-16 sequence and the observed T_2 times are otherwise independent of the initial nuclear phase.
[22] D. W. Leung, I. L. Chuang, F. Yamaguchi, and Y. Yamamoto, Phys. Rev. A **61**, 042310 (2000).
[23] E. D. Ostroff and J. S. Waugh, Phys. Rev. Lett. **16**, 1097 (1966); D. Suwelack and J. S. Waugh, Phys. Rev. B **22**, 5110 (1980).
[24] A. S. Verhulst, D. Maryenko, Y. Yamamoto, and K. M. Itoh, Phys. Rev. B **68**, 054105 (2003).
[25] K. Takyu, K. M. Itoh, K. Oka, N. Saito, and V. I. Ozhogin, Jpn. J. Appl. Phys., Part 2 **38**, L1493 (1999).
[26] S. Idziak and U. Haeberlen, J. Magn. Reson. (1969-1992) **50**, 281 (1982).
[27] R. G. Shulman and B. J. Wyluda, Phys. Rev. **103**, 1127 (1956); G. Lampel and I. Solomon, C. R. Hebd. Seances Acad. Sci. **258**, 2289 (1964); B. Sapoval and D. Lepine, J. Phys. Chem. Solids **27**, 115 (1966).
[28] J. E. Mooij *et al.*, Science **285**, 1036 (1999); I. Chiorescu, Y. Nakamura, C. J. P. M. Harmans, and J. E. Mooij, *ibid.* **299**, 1869 (2003).
[29] Y. Makhlin, G. Schön, and A. Shnirman, Nature (London) **398**, 305 (1999); Yu. A. Pashkin *et al.*, *ibid.* **421**, 823 (2003); D. Vion *et al.*, Science **296**, 886 (2002).
[30] Y. Yu, S. Han, X. Chu, S.-I. Chu, and Z. Wang, Science **296**, 889 (2002); A. J. Berkley *et al.*, *ibid.* **300**, 1548 (2003).
[31] H. Kessemeier and R. E. Norberg, Phys. Rev. **155**, 321 (1967).
[32] U. Haeberlen, J. D. Ellet, Jr., and J. Waugh, J. Chem. Phys. **55**, 53 (1971).
[33] R. D. Black, M. B. Weissman, and P. J. Restle, J. Appl. Phys. **53**, 6280 (1982); Phys. Rev. B **28**, 1935 (1983).
[34] R. Kubo and K. Tomita, J. Phys. Soc. Jpn. **9**, 888 (1954).
[35] This speculation is suggested by the temperature dependence of T_1 in silicon with less than about $10^{15}\mathrm{cm}^{-3}$ shallow dopants (Ref. 6); its exponential form suggests an important role for thermally activated carriers.
[36] G. M. Zhidomirov and K. M. Salikhov, Sov. Phys. JETP **29**, 1037 (1969); R. de Sousa and S. Das Sarma, Phys. Rev. B **68**, 115322 (2003).
[37] R. de Sousa (unpublished).
[38] This is in contrast to models where a single electron spin (Ref. 36) or Josephson junction qubit [E. Paladino, L. Faoro, G. Falci, and R. Fazio, Phys. Rev. Lett. **88**, 228304 (2002)] couples to many bistable fluctuators, and the *fastest* decaying components contribute most to the final signal, which is calculated as a product over fluctuators rather than a sum.
[39] P. R. Bevington and D. K. Robinson, *Data Reduction and Error Analysis for the Physical Sciences*, 2nd ed. (McGraw-Hill, New York, 1992).
[40] P. Dutta, P. Dimon, and P. M. Horn, Phys. Rev. Lett. **43**, 646 (1979).
[41] R. Vrijen *et al.*, Phys. Rev. A **62**, 012306 (2000).
[42] J. M. Taylor, C. M. Marcus, and M. D. Lukin, Phys. Rev. Lett. **90**, 206803 (2003).
[43] D. P. Burum, M. Linder, and R. R. Ernst, J. Magn. Reson. (1969-1992) **44**, 173 (1981).
[44] B. Cowan, *Nuclear Magnetic Resonance and Relaxation* (Cambridge University Press, Cambridge, U.K. 1997).